Journal of Energy Storage 71 (2023) 108089

Contents lists available at ScienceDirect

Journal of Energy Storage

journal homepage: www.elsevier.com/locate/est

Research papers

Multi-objective optimization of a metal hydride reactor coupled with phase change materials for fast hydrogen sorption time

Serge Nyallang Nyamsi [a,*], Ivan Tolj [b], Sivakumar Pasupathi [a]

[a] HySA Systems Competence Centre, South African Institute for Advanced Materials Chemistry (SAIAMC), University of the Western Cape, Bellville 7535, South Africa
[b] Faculty of Electrical Engineering, Mechanical Engineering and Naval Architecture, University of Split, R Boskovica 32, 21000 Split, Croatia

ARTICLE INFO

Keywords:
Metal hydride
Passive heat management
Phase change materials
Multi-objective optimization

ABSTRACT

Recently, the utilization of phase change materials (PCM) for the heat storage/recovery of the metal hydride's reaction heat has received increasing attention. However, the poor heat management process makes hydrogen sorption very slow during heat recycling. In this work, the H_2 charging/discharging performance of a metal hydride tank (MHT) filled with $LaNi_5$ and equipped with a paraffin-based (RT35) PCM finned jacket as a passive heat management medium is numerically investigated. Using a two-dimensional mathematical model validated with our in-house experiments, the effects of design parameters such as PCM thermophysical properties and the fin size on hydrogen charging/discharging times of the MHT are investigated systematically. The results showed that the PCM's melting point and apparent heat capacity have a conflicting impact on the hydrogen sorption times, i.e., the low melting point and high specific heat capacity reduce the H_2 charging time. In contrast, the hydrogen discharging time follows the opposite trend. As a result, a multi-objective optimization was conducted to simultaneously minimize the H_2 charging/discharging times using the thermal properties and size of the PCM. The optimum solutions selected from the Pareto front show that the PCM melting point should be around 42–43 °C for fixed hydrogen ab/desorption pressures of 10/1.5 bar. Moreover, the comparison between the MHT-PCM using the optimized PCM and reference PCM showed that the former reduced the hydrogen charging/discharging times by 48.6 % and 4 %, respectively. At the same time, the hydrogen storage efficiency of the optimal design is 100 % as compared to 96 % for the reference design. Besides, among the practical PCMs, inorganic PCMs (salt hydrates and eutectics) display favorable hydrogen charging time below 3000 s at the expense of hydrogen discharging time (above 7000 s) in our case study.

1. Introduction

Hydrogen has been a promising green energy vector for many years. It can be produced from a surplus of available energy and used later with fuel cells for electricity production. As a result, a formidable amount of research has been undertaken to date. One of the main challenges of its take-off in many practical applications is its storage [1]. As hydrogen is the lightest known gas, its storage in high density is still a conundrum. Solid-state hydrogen storage in metal hydrides is the most appealing option compared to commercially available options (e.g., compressed and liquid H_2) because of its compelling attributes, such as safety, high hydrogen capacity, and energy efficiency, among others [2]. Despite these advantages, hydrogen storage systems utilizing well-known metal hydrides still fall short of the targets for mobile applications set by the US Department of energy [3].

The reaction between a metal and hydrogen involves a great deal of thermal energy (heat). As a result, heat should be removed or added efficiently for the reaction to proceed smoothly and fast [4]. For this reason, the design and development of metal hydride-based hydrogen storage fall into devising an efficient thermal management strategy [5,6]. Due to the low thermal conductivity of metal hydrides (<1 $W{\cdot}m^{-1}{\cdot}K^{-1}$), thermal management methods comprise thermal conductivity enhancements [5] (e.g., metal matrices [7], metal foams [8,9] or expanded natural graphite ENG [10]) or the insertion of heat exchangers such as finned tube [4], heat pipes [11,12], multi-tubes [13], helical tube [14] etc. Although these methods of heat transfer improvement have been popularly used in the literature, it is noticed that little has been discussed about the entailed external energy required due to the pumping power of the heat transfer fluid (HTF) in the tubes. Besides, external heat should be provided to the system to desorb the previously stored H_2. However, this heat depends on the material under

* Corresponding author.
E-mail address: nyamsiserge@gmail.com (S.N. Nyamsi).

https://doi.org/10.1016/j.est.2023.108089
Received 26 January 2023; Received in revised form 30 May 2023; Accepted 13 June 2023
Available online 28 June 2023

Nomenclature

Symbols

C_p	heat capacity ($J{\cdot}kg^{-1}{\cdot}K^{-1}$)
ΔCp	PCM heat capacity difference between liquid and solid phase ($J{\cdot}kg^{-1}{\cdot}K^{-1}$)
E_a, E_d	activation energy, ab/desorption ($J{\cdot}mol^{-1}$)
f	PCM melted fraction
$F_{i,j}$	objective function
FS	fin spacing (m)
g_X	uncertainty on the hydrogen charging/discharging time (%)
ΔH	reaction heat ($J{\cdot}mol^{-1}$ H_2)
k	PCM sharper transition parameter, Eq. (7)
k_a, k_d	the reaction rate constant, abs/des (s^{-1})
K_{eff}	effective bed permeability (m^2)
L	length (m)
M_g	H_2 molecular weight ($kg{\cdot}mol^{-1}$)
$\vec{n}$	outward normal vector
p, P	pressure (Pa)
R_g	universal gas constant ($J{\cdot}mol^{-1}{\cdot}K^{-1}$)
R, r	radius, radial coordinate (m)
ΔS	entropy change of the reaction ($J{\cdot}mol^{-1}{\cdot}K^{-1}$)
t	time (s)
T	temperature (K)
ΔT_{abs}, ΔT_{des}	heat transfer driving force during the absorption and desorption (K)
ΔT_{tr}	PCM transition, mushy zone (K)
V	volume (m^3)
$\vec{V}$	velocity ($m{\cdot}s^{-1}$)
wi	objective function weight (preference factor), Eq. (26)
wt.	H_2 weight capacity
z	height coordinate (m)
ΔX	uncertainty on parameter X, Eq. (24)

Greek letters

α	reacted fraction
β	factor in Eq. (23)
δ	fin thickness (m)
Δ	Euclidian distance between the ideal solution and optimal solution on the Pareto front
ε	bed porosity
ϕ	fin volume fraction (%)
λ	thermal conductivity ($W{\cdot}m^{-1}{\cdot}K^{-1}$)
μ	dynamic viscosity (Pa·s)
ρ	density ($kg{\cdot}m^{-3}$)

Subscript

a, abs	absorption
b	bed
d,des	desorption
eq	equilibrium
eff	effective
fin	extended surface
g	gas
in	inlet
MH	metal hydride
out	outlet
PCM	phase change material
w	wall

investigation. For example, taking into account the most utilized AB_2, AB_5-hydrides, and MgH_2, the H_2 desorption heat accounts for 10, 12.5 and 30 % of H_2 LHV (lower heating value: 240 kJ/mol-H_2), respectively [15,16]. Therefore, devising a system that could passively store and restore this heat is of great interest from an energy efficiency viewpoint. Phase change materials (PCMs) can play this pivotal role since they can hold a significant amount of heat in a narrow temperature range. In a coupling MH tank (MHT)-PCM scenario, the PCM absorbs the reaction heat during the H_2 storage in MH by melting. During the H_2 discharging from the MH, the PCM gives up the previously stored heat by freezing [16].

Only a few studies have proposed and investigated the performance of MHT-PCM systems for hydrogen storage applications in the literature. In the earlier study discussing this system, Garrier et al. [16] experimentally investigated the performance of an MHT-PCM system based on MgH_2 and a eutectic mixture of Mg—Zn PCM. The H_2 desorption from a pilot tank containing about 7000 NL of H_2 was discussed. It was shown that the H_2 desorption was completed in 3 h with a storage efficiency of 70 %. It was also noted that the decrease in storage efficiency was due to the thermal loss from the PCM and the high operating temperature of MgH_2 (370 °C). Several works have been undertaken following this experimental work to optimize the system. Mellouli et al. [17] studied numerically the performance of high-temperature MHT equipped with a PCM heat exchanger, presented by the experiments by Garrier et al. [16].

Moreover, they studied the effects of the system configuration (cylindrical and spherical) on the overall performance of MHT-PCM. The results showed that the spherical design performs better than the cylindrical one. Darzi et al. [18] investigated numerically the performance of a long tubular metal hydride reactor inserted in a PCM jacket for fuel cell applications. The findings showed that the rates at which PCM melts or solidifies are a function of H_2 supply and discharge pressures. Also, the bed porosity significantly impacted the melting and freezing fraction of the PCM; e.g., in the desorption process, 67 %, 83 %, and 95 % of liquid PCM freezes for bed porosities of 0.6, 0.5, and 0.4, respectively. Moreover, improving the thermal conductivity of PCM by inserting metal foams has been shown to significantly reduce the H_2 charging and discharging time. El Mghari et al. [19] and Tong et al. [20] studied the performance of an MHT equipped with a PCM jacket. A 2D model was developed and validated for H_2 absorption and desorption. The effects of thermo-physical properties of PCM on the H_2 ab/desorption were studied in detail. The results showed that the latent heat of PCM affects more the MHT performance than the thermal conductivity does. Ben Maad et al. [21] investigated the heat and mass transfer phenomena on an MHT incorporating a PCM heat exchanger. They formulated a model of PCM which used a smooth Heaviside step function to describe the liquid fraction of the PCM. The findings revealed that the higher the PCM latent heat, the higher the hydrogen absorbed in the MHT. Besides, a higher thermal conductivity of PCM quickens the hydrogen absorption process. Ben Maad et al. [22] reported numerically the H_2 desorption performance of a high-temperature MHT (Mg_2NiH_4) incorporating a PCM jacket. Their model considered the radiative heat transfer, which was neglected in previous works studying the same high-temperature metal hydrides operating at temperatures higher than 300 °C. The appropriate PCM fitted for the application was a metallic eutectic mixture Mg—Zn ($Mg_{69}Zn_{29}Al_3$) with a melting point of around 600 °C. The results showed that the time required to desorb all the Hydrogen capacity of the reactor did not exceed 2.5 h. Nyallang et al. [23] numerically investigated the impact of integrating a PCM jacket into a two-tank thermal energy storage system for industrial waste heat recovery. The effects of the thermophysical properties of the PCM and the PCM jacket size on the performance indicators such as energy density,

power output, and energy recovery efficiency of the heat storage system were systematically analyzed and discussed. The results showed that these performance indicators significantly impacted the performance indicators among PCM properties, the melting point, the latent heat of fusion, the density, and the thermal conductivity. Miled et al. [24] investigated the MHT-PCM systems for water pumping. The results showed that the PCM thermal properties significantly affect the water head and the volume pumped. Yao et al. [25] proposed a modified model of coupled MHT-PCM systems that analyzes a continuous absorption/desorption process. The revised model proved to be more accurate than the traditional one.

Furthermore, the parametric study showed that the melting point of the PCM significantly impacts the H_2 storage efficiency. On the other side, improving the thermal conductivity of PCM by ENG boosts the H_2 storage efficiency from 47 to 72 %. Ye et al. [26] suggested an MHT-PCM system comprising PCM disks sandwiched between MH bed disks. They showed that this configuration reduces the overall thermal resistance between the media. Another non-conventional system configuration was proposed by Alqahtani et al. [27]. It consisted of MH sandwiched between two layers of PCM. To improve the performance further, they [27] investigated the effect of using multiple layers of PCM with different latent heat and melting/freezing points.

In general, pristine PCMs (e.g., paraffin waxes) have a very low thermal conductivity [28] ($<0.3\ W{\cdot}m^{-1}{\cdot}K^{-1}$) relative to that of processed metal hydrides ($\sim 1\ W{\cdot}m^{-1}{\cdot}K^{-1}$). Therefore, the conductive heat transfer mode in MHT-PCMs systems is limited by the thermal resistance of the PCM media. Thus, scholars usually apply two techniques. The first one consists of adding nanoparticles of carbon-based materials [29,30] or metal oxides (Al_2O_3, MgO, SnO_2, and SiO_2) [31]. This technique can improve thermal conductivity by up to 170–190 % [30]. However, this method improves thermal conductivity and may modify thermophysical properties such as density, heat capacity, and latent heat. For example, inserting 30 wt% of graphite in paraffin decreases the latent heat from 226 $kJ{\cdot}kg^{-1}$(pure paraffin) to 152.5 $kJ{\cdot}kg^{-1}$ [29]. The melting point increases by up to 6 °C if 11.4 vol% of graphite is added to a paraffin based PCM [30].

The second method uses extended surfaces of metals with very high thermal conductivity. These include metal foams [32–35] and fins [36–45] with different shapes (radial, longitudinal, pin, tree-like, etc.). Metal foams can improve thermal conductivity by 120.5 [33] to 12,300 % [34]. Moreover, using metal foam in PCMs allows uniform temperature distribution [35]. Conversely, fins provide a heat transfer path from a heat source to a heat sink while improving the PCM's thermal conductivity. Numerical and experimental studies showed that the melting of PCMs is governed by two heat transfer mechanisms: conduction and natural convection. The heat transfer by conduction generally predominates at the early stage of the melting. At the same time, natural convection dominates at a higher melting fraction of PCM, thereby quickening the melting process [42]. However, PCM systems adopting heat transfer enhancement, such as fins and metal foams, showed that natural convection could be suppressed in some scenarios. Li et al. [43] investigated experimentally and numerically the effect of metal foams' properties on a paraffin-based PCM's melting/freezing performance. They showed that the foam matrix reduces the melted PCM flow. As a result, the effect of natural convection is lessened.

Further heat transfer enhancement by conduction hinted at a reduction of foam porosity. Likewise, some numerical and experimental studies on heat storage/discharging using PCM/fins showed that only heat conduction is the predominant heat transfer mechanism [42,44,45]. Fins, especially transversal or annular fins, generally divide the PCM domains into subdomains in which the buoyancy-driven convection is weakened.

The above discussion analysis shows momentum in investigations of MHT-PCMs systems though several studies have been reported so far. However, these research works have the following shortcomings which require in-depth investigation: (1) the systems presented are of small scales (size) except the recent study by Chibani et al. [31], (2) only a selected PCM is investigated at the time, (3) a few works systematically investigated the H_2 desorption from the metal hydride reactors for hydrogen supply to fuel cells [46], (4) there is a lack of experimental studies to understand further (validated) the numerical behavior of MHT-PCM systems.

Since the PCM solely provides passive thermal management, such systems' H_2 absorption/desorption time is very long (hours). As a result, such systems can only fit the scope of stationary H_2 storage applications, whereby the hydrogen storage time is not as crucial as the hydrogen desorption time. Hydrogen desorption should provide a sufficient H_2 flow rate when such systems are coupled with fuel cells to sustain a constant power output. The previous research works [17–22,47] only studied the effects of some selected thermophysical properties of PCM on the performance of the hydrogen storage systems without giving the properties of the ideal PCM that would lead to an optimal design of MHT-PCM hydrogen storage system. Therefore, in this study, the performance of an MHT-PCM system is systematically investigated. The effects of the thermophysical properties of PCM on the H_2 charging and discharging times are analyzed in detail. Furthermore, the impact of heat transfer enhancement by inserting extended surfaces such as fins on the system performance is also presented. Finally, a multi-objective optimization will be formulated to determine the optimal thermophysical properties that simultaneously minimize the H_2 charging/discharging times. A 2D mathematical model will be formulated and developed to accomplish these goals. Further, the selection of 2D axis-symmetry significantly reduces the computational load, which is more observable in the optimization process [48]. It was shown that 2D axis-symmetry could efficiently capture the physical behavior of a 3D mathematical model of the same system with minimum error.

2. Numerical model

2.1. Physical model

Fig. 1 portrays the MHT-PCM system for stationary fuel cell applications. During the heat charging, the metal hydride tank is charged with H_2 from an H_2 supply bottle. The heat of the reaction is stored in the PCM. When power is needed from the fuel cell, H_2 is discharged from the MHT by absorbing the heat from the PCM. As a result, the PCM solidifies while giving up heat. The physical model consists of a $LaNi_5$-based metal hydride tank integrated with a reference PCM (Rubitherm RT35) jacket (MHT-PCM jacket) [18]. This system geometry is the most investigated in the literature. However, here we have added transversal fins to reduce the thermal resistance of heat conduction from PCM to MH or vice versa. A previous study demonstrated that the modified geometry outperformed the conventional one during the hydrogen desorption process [46]. Therefore, the PCM's thermal conductivity is enhanced by adding × vol% of aluminum fins while keeping in mind the tradeoff between increasing thermal conductivity and decreasing the amount of PCM (latent thermal energy). The size of the hydrogen storage system made in structural aluminum (6061-T6) is given in Table 1.

2.2. Governing equations

The following reasonable assumptions are laid for the metal hydride bed and PCM jacket:

- The properties of metal hydride are uniform during the transient process.
- The thermal equilibrium between the hydrogen and solid hydride is assumed for the porous metal hydride bed.
- The hysteresis and slope factors in the equilibrium pressure are neglected.
- The reaction of metal hydrides is described with the first-order kinetics

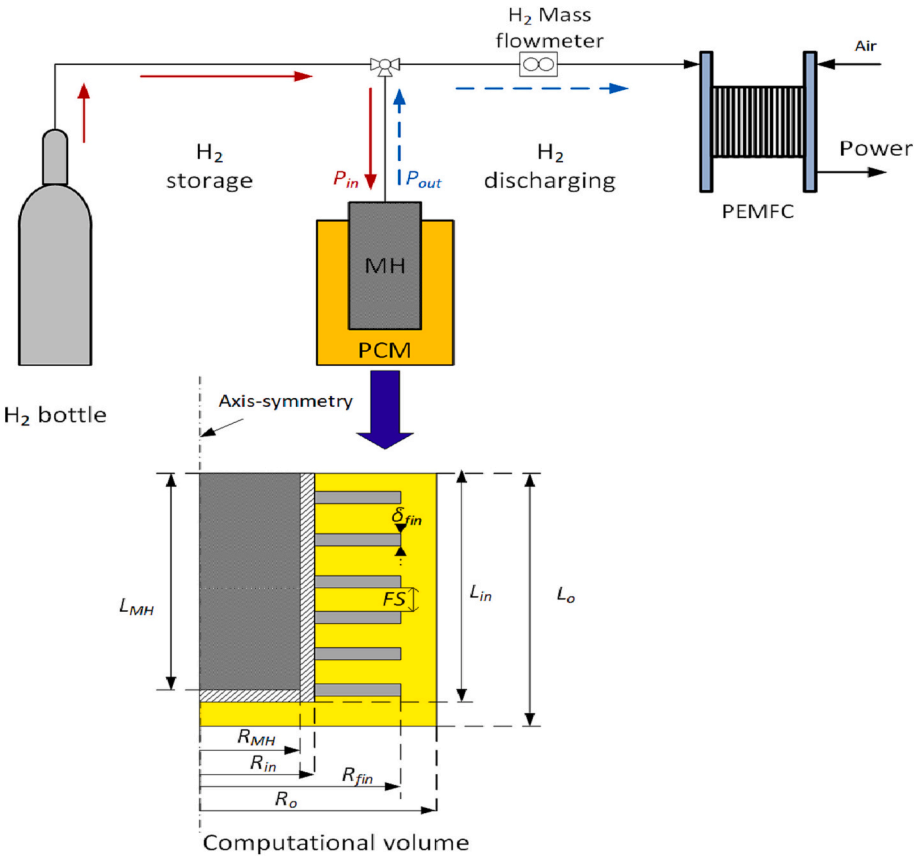

Fig. 1. Metal hydride tank (MHT)-phase change materials systems (PCM) for stationary applications.

Table 1
Sizing and the thermal properties of structural aluminum (6061-T6).

Parameters/unit	Value
MH reactor, R_{MH}/m	0.02
MH reactor height L_{MH}/m	0.4
Wall thickness, R_{in}-R_{MH}/m	0.002
PCM thickness, R_o-R_{in}/m	0.023
PCM height, L_o/m	0.412
Fin length, L_{fin}/m	0.01–0.022
Fin spacing, FS/m	0.01
Fin thickness, δ_{fin}/m	0.002
Density, ρ/kg·m^{-3}	2700
Specific heat capacity, C_p/J·kg^{-1}·K^{-1}	897
Thermal conductivity, λ/W·m^{-1}·K^{-1}	166

- The thermo-physical properties (density, latent heat, and thermal conductivity), besides the apparent heat capacity of the phase change materials, are assumed to be fixed [34,35].
- The buoyancy effect due to the volumetric forces of PCM is neglected. Therefore, the impact of the natural convection mechanism on the PCM melting is insignificant because of the presence of transversal fins [42,44,45].

The model starts with the energy balance of the metal hydride/hydrogen inside the reactor, which is computed as follows:

$$(\rho C_p)_{eff}\frac{\partial T_{MH}}{\partial t}+\nabla\cdot\left(\rho_g C_{pg}\vec{V}T_{MH}\right)=\lambda_{eff}\nabla^2 T_{MH}+\frac{(1-\varepsilon)}{M_g}\rho_{MH}wt\frac{d\alpha}{dt}\Delta H \quad (1)$$

where the compounded heat capacity and the thermal conductivity are evaluated by the porous media mixing rule:

$$(\rho C_p)_{eff}=\varepsilon\rho_g C_{pg}+(1-\varepsilon)\rho_{MH}C_{pMH} \quad (2)$$

$$\lambda_{eff}=\varepsilon\lambda_g+(1-\varepsilon)\lambda_{MH} \quad (3)$$

The local temperature of the reactor wall and metal fins is formulated by heat conduction with no heat source as follows:

$$(\rho C_p)_{w/fin}\frac{\partial T_{w/fin}}{\partial t}=\lambda_{w/fin}\nabla^2 T_{w/fin} \quad (4)$$

Likewise, the temperature variation in the PCM domain is formulated by the apparent heat capacity model, which is expressed [17,18]:

$$\rho_{pcm}C_{p,eff}(T_{pcm})\frac{\partial T_{pcm}}{\partial t}=\lambda_{pcm}\nabla^2 T_{pcm} \quad (5)$$

The apparent heat capacity of the mixture is a linear function of the melting fraction of the phase change material, defined as follows:

$$\rho_{pcm}C_{p,eff}(T)=\rho_{pcm}\left(C_{pPCM}+\Delta H_{pcm}\frac{df(T_{pcm})}{dT_{pcm}}\right) \quad (6)$$

where $C_{pPCM}=C_{p,s}+f\cdot\Delta C_p$ with ΔC_p is the difference between the liquid and solid heat capacity. In Eq. (6), the density of PCM is assumed to be the mean density between the liquid and solid phases. The rate of liquid fraction with temperature can be approximated by a smoothed Gaussian distribution as [21,22] or the rate of sigmoid function as given by Maad et al. [22]:

$$f(T_{pcm})=\frac{1}{1+exp(-k(T_{pcm}-T_m))} \quad (7)$$

where k (sharper transition parameter [22]) depends on the phase change transition ΔT_{tr}, T_m is the melting point, which is generally the peak temperature of the melting profile of a PCM. The rate of the liquid fraction can be written as:

$$\frac{df(T_{pcm})}{dT_{pcm}} = kf(1-f) \tag{8}$$

where ΔT_{tr} and T_m are the mushy zone interval (phase transition range) and the melting point (which is the peak temperature of the melting profile of a PCM).

The mass balance gives the change of hydrogen density in the metal hydride bed

$$\varepsilon\frac{\partial \rho_g}{\partial t} + \nabla\cdot\left(\rho_g \overrightarrow{V}_g\right) = -(1-\varepsilon)\rho_{MH} wt \frac{d\alpha}{dt} \tag{9}$$

where Darcy's law describes the gas speed in the porous bed

$$\overrightarrow{V_g} = -\frac{K_{eff}}{\mu_g}\nabla p_g \tag{10}$$

The ideal gas law obtains the relation between the gas pressure and its density:

$$p_g = \frac{\rho_g R_g T_{MH}}{M_g} \tag{11}$$

The first-order kinetic model reasonably describes the reaction kinetics of low-temperature metal hydrides ($TiMn_2$ and $LaNi_5$) [21,31] as follows:

For the absorption process

$$\frac{d\alpha}{dt} = k_a exp\left(\frac{E_a}{R_g T_{MH}}\right) ln\left(\frac{p_g}{p_{eq}}\right)(1-\alpha) \tag{12}$$

For the desorption process

$$\frac{d\alpha}{dt} = k_d exp\left(\frac{E_d}{R_g T_{MH}}\right)\left(\frac{p_g - p_{eq}}{p_{eq}}\right)\alpha \tag{13}$$

The equilibrium pressure is expressed as follows:

$$ln\left(\frac{p_{eq}}{p_0}\right) = \frac{\Delta H}{R_g T_{MH}} - \frac{\Delta S}{R_g} \tag{14}$$

Initial conditions

Initially, the system is at a constant room temperature.

$$T(r,z,t=0) = T_{pcm}(r,z,t=0) = T_{w/fin}(r,z,t=0) = 20^{\circ}\mathrm{C} \tag{15}$$

$$p_g(r,z,t=0) = p_{eq}(T = 20^{\circ}C) = 1.96\ bar \tag{16}$$

The PCM is in the solid phase, and the metal hydride is fully dehydrogenated

$$\alpha(r,z,t=0) = f(r,z,t=0) = 0 \tag{17}$$

where r and z are the radius and the height, respectively.

Boundary conditions

Since there is no heat convection involved in this physical model, only the continuity of the conductive heat is considered as follows:

The general conduction/conduction heat continuity between two interfaces, 1 and 2, is expressed with the following equation

$$(\lambda_1 \nabla T_1 - \lambda_2 \nabla T_2)\cdot\vec{n} = 0 \tag{18}$$

The PCM jacket is fully insulated:

$$\left(\frac{\partial T}{\partial r}\right)_{r=r_{PCM}} = 0 \tag{19}$$

The H_2 absorption and desorption pressures are as follows:

$$P_{in} = 10\ bar, P_{out} = 1.5\ bar \tag{20}$$

The pressure condition was modified in one equation to allow for a continuous absorption/desorption simulation process by:

$$P_b = P_{in}(t \le t_{abs}) + \left\{P_{in} - \frac{(P_{in} - P_{out})}{t_s}(t - t_{abs})\right\}(t_{abs} < t < t_{abs} + t_s) + P_{out}(t \ge t_{abs} + t_s) \tag{21}$$

The second term (curly bracket) in the right-hand side of Eq. (21) allows the pressure to decrease linearly from P_{in} to P_{out} without causing a convergence problem during the simulation course. During this period (storage time, t_s), the source term is switched off due to the chemical reaction. As a result, the combined source term for a chemical reaction is expressed as:

$$\frac{d\alpha}{dt} = \left(\frac{d\alpha}{dt}\right)_{abs}(t \le t_{abs}) + \left(\frac{d\alpha}{dt}\right)_{des}(t \ge t_{abs} + t_s) \tag{22}$$

2.3. Selection of the PCMs thermal properties

The selection of PCMs for MHT-PCM systems is not straightforward. Since temperature gradients drive the metal hydride performance, the difference between the MH operating temperature and the heat exchange medium (PCM) should be high. Therefore, the choice of the melting point of PCM should depend on the absorption/desorption equilibrium temperatures. The equilibrium pressure is intimately linked to the H_2 ab/desorption pressures through the Van't Hoff equation, Eq. (14). A typical Van't Hoff diagram of a metal hydride is plotted in Fig. 2, where the hysteresis is neglected for illustration purpose.

The PCM melting point should be located within the range [T_{des}, T_{abs}] with:

$$T_m = T_{des} + \beta(T_{abs} - T_{des}), 0 < \beta < 1 \tag{23}$$

If the difference between the PCM melting point and T_{abs} (ΔT_{abs}) is higher, the absorption process is faster than the desorption process. Conversely, if ΔT_{des} is higher, the H_2 desorption process is shorter than the absorption one. Previous studies [49,50] recommended a melting point in the middle of the range [T_{des}, T_{abs}], i.e., $\beta = 0.5$. Taking $LaNi_5$ as the working material, the absorption and desorption temperatures T_{abs} and T_{des} corresponding to H_2 pressures given in Eq. (20) are 64.6 and

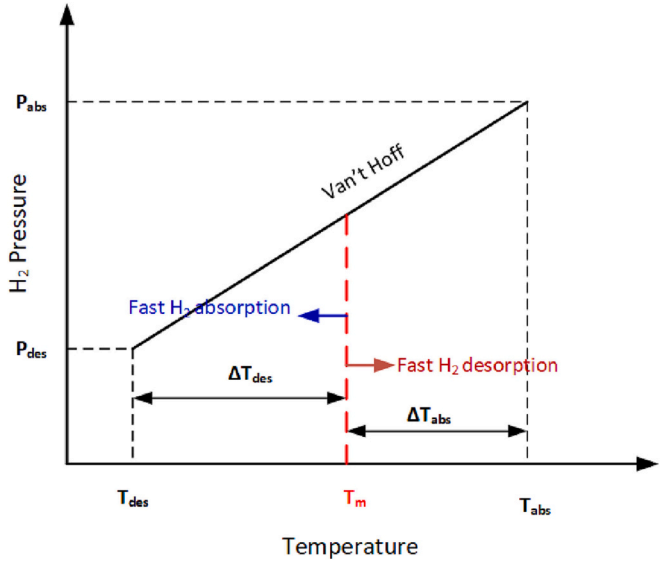

Fig. 2. Selection of the PCM melting point based on the equilibrium pressures of H_2 absorption and desorption.

Table 2
Thermophysical properties of selected organic/inorganic phase change materials.

PCM	ρ_s/ρ_l (kg·m^{-3})	T_m (°C)	Cp_s/Cp_l J·kg^{-1}·K^{-1}	ΔH_{pcm} (kJ/kg)	λ_s/λ_l (W·m^{-1}·K^{-1})
RT35	880/760	34–35	1800/2400	170	0.24/0.20
RT45	880/760	44–46	1800/2400	170	0.24/0.20
$LiNO_3$·3H2O	2140/1780	30–31	1730/2770	296	1.32/0.58
Na_2SO_4·10H_2O	1485/1420	32.5–33.5	1440/2570	251	1.23/0.54
$Zn(NO_3)_2$·6H_2O	1937/1700	36.4–37	2260	147	−/0.47
SP29Eu	2000	29–30	2500	175	0.6
SP32Eu	2000	32–33	2000/2500	175	1.05/0.7

13.73 °C, respectively. As a result, the optimal PCM's melting point is around 39 °C. Besides the melting point, other important PCM thermal properties, such as latent heat of fusion, heat capacity, density, etc., affect the H_2 charging and discharging times. To understand the effect of PCM's thermophysical properties on the charging and discharging time, a preliminary sensitivity analysis is performed by the calculation of uncertainty using gradient-based methods defined as follows:

$$g_{Xi} = \left(\frac{\Delta t_{ch,dis}}{\left(t_{ch,dis}\right)_{base}}\right)_{X_i} = \frac{\left(\frac{\partial t_{ch,dis}}{\partial X_i}\right)\cdot \Delta X_i}{\left(t_{ch,dis}\right)_{base}} \tag{24}$$

The magnitude of g_{xi} defines the effect that the PCM's intrinsic property (X_i) has on the objective function $t_{ch,dis}$. ΔX is the PCM thermophysical parameter increment from the baseline (RT35). For this study, we assume an increment of 10 %. $\left(t_{ch,dis}\right)_{base}$ is the system's hydrogen charging and discharging time when the reference PCM (RT35) is utilized. Furthermore, unless specified otherwise, t_{ch} and t_{dis} are the process times at $\alpha = 0.9$ and $\alpha = 0.1$, respectively.

Practically, three types of PCMs can be utilized for the thermal management of low-temperature metal hydrides, namely organic (e.g., paraffin waxes), inorganic (salt hydrates), and eutectic (mixture of organic/inorganic or both). Paraffin has the benefits of high heat of fusion and melting congruently. However, given their low density (<1 kg·L^{-1}), their volumetric energy density is lower than salt hydrates'. The only drawbacks of salt hydrates are their corrosiveness, the high supercooling effect (the freezing point is lower than the melting point), and the incongruent melting. Table 2 lists a few selected PCMs compiled from reference data [18, 25, 46, 50], which have been tested for the hydrogen storage performance.

3. Experimental setup for a numerical validation

Fig. 3 depicts the experimental setup. It consists of a Sievert-type apparatus to measure the reactor's volumetric change of hydrogen. The metal hydride tank (MHT) is inserted in a cylindrical vial containing coconut oil, acting as a phase change material (PCM). Coconut oil is a bio PCM made of unsaturated fatty acids, readily available daily. It is cheaper than commercially available paraffin waxes. The average price of coconut oil in South Africa was around ZAR60/L (2021 price, where the exchange rate is US$1 = 16 ZAR). About 30.5 g of AB2-type hydride was inserted in a stainless-steel reactor. The choice of this material for experimental validation was due to its availability in our laboratory. Our laboratory has a huge experience in the manufacturing and the testing of AB2 type hydrides for hydrogen storage and compression applications [51,52]. During the H_2 absorption experiments, the hydride was in contact with ~15 bar hydrogen-filled in a calibrated reference volume of 604 ± 2.29 cm^3. The amount of hydrogen absorbed by the hydride material was calculated using the pressure change in the reference volume and the ideal gas equation. The temperatures at the reactor core and wall were measured using K-type thermocouples, T_{MH}, and T_{PCM}, respectively as depicted in Fig. 3. The sizing of the computational volume is also given in the figure (note the dimensions in mm).

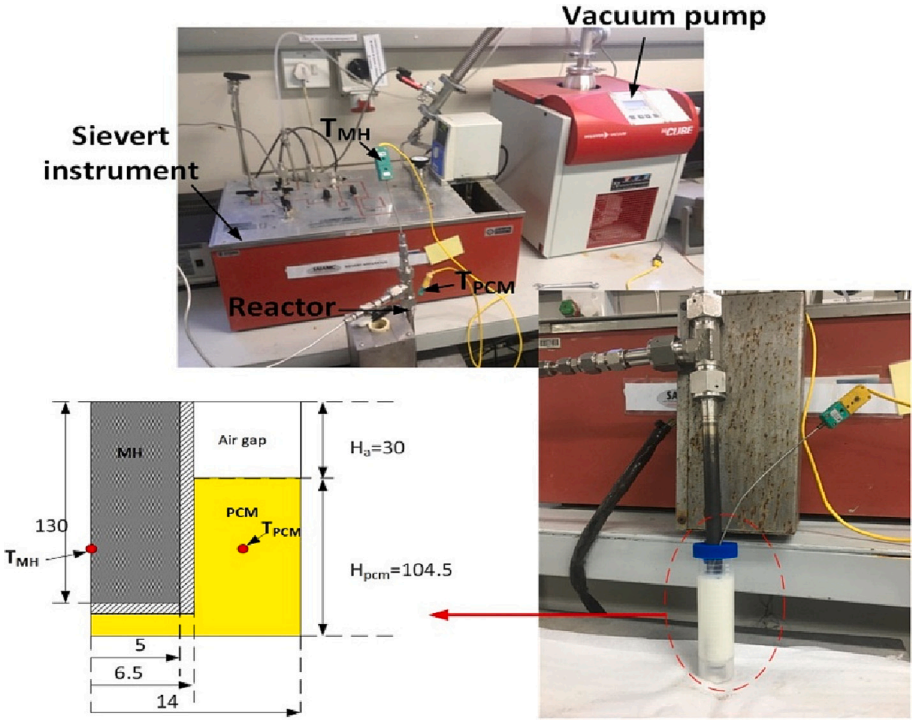

Fig. 3. Experimental test rig for testing a small MHT-PCM system.

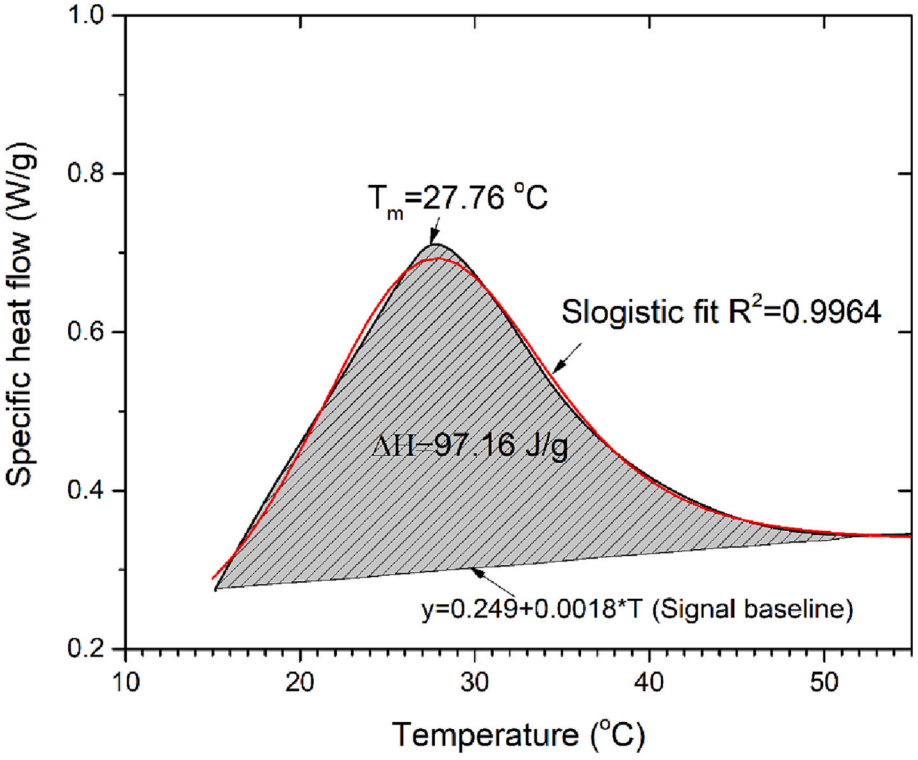

Fig. 4. Specific heat capacity of coconut oil by calorimetry at 5 K/min; The peak is fitted by the derivative of a sigmoid (S-logistic) function.

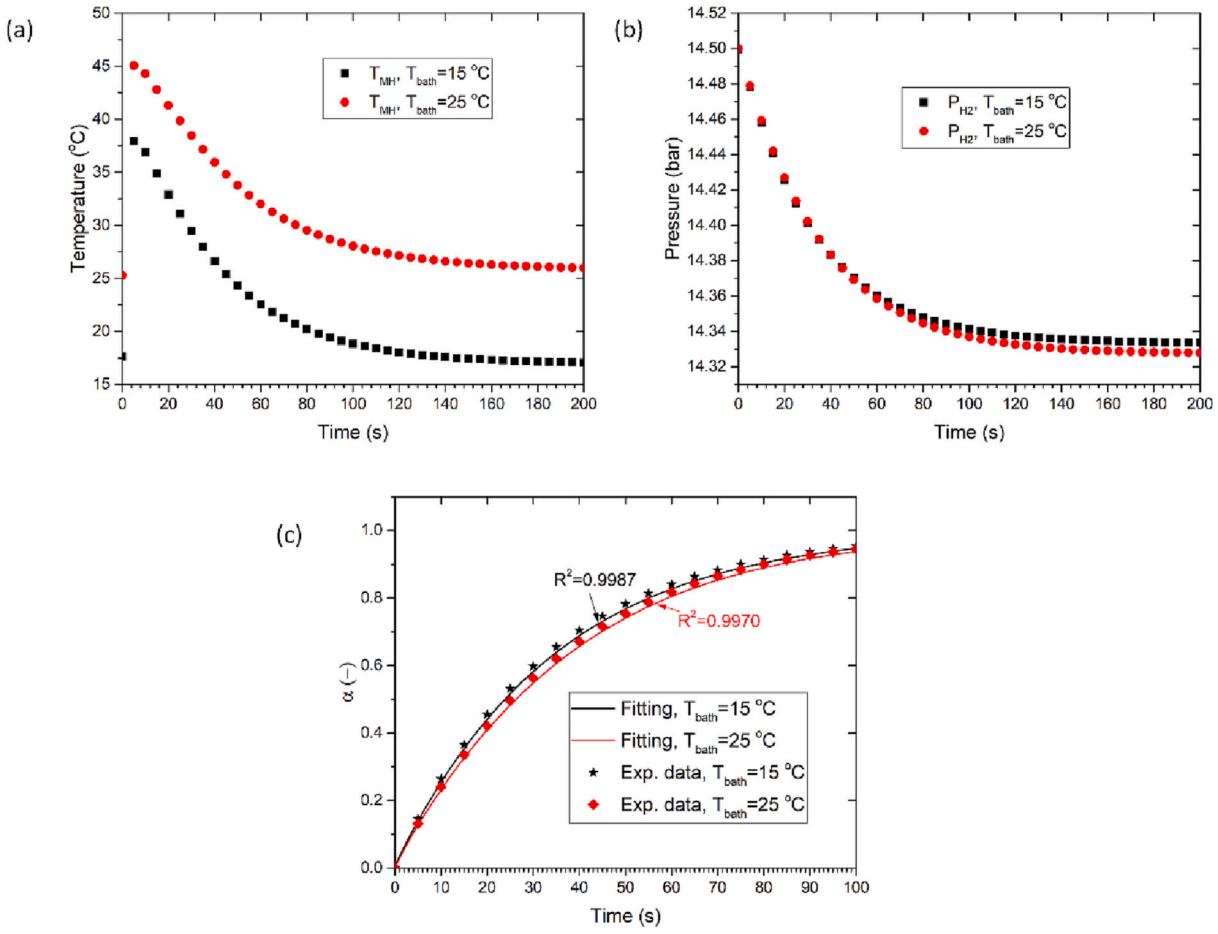

Fig. 5. Curve fitting of H_2 sorption kinetics of the used AB2-type hydride.

Table 3
Thermo-physical properties of AB2-type hydrides used for model validation and $LaNi_5$ used for sensitivity analysis and optimization.

Parameter/unit	$Ti_{0.55}Zr_{0.45}$ $(FeCrMnNiV)_2$.	$LaNi_5$ [18–20]
Heat of reaction/ kJ·mol^{-1}	22.4	30.5
Entropy change/ J·mol^{-1}·K^{-1}	88.9 (abs)	108
Activation energy, abs/kJ·mol^{-1}	21.400 (abs)	21.17/16.47
Rate constant, abs-des/s^{-1}	169 (abs)	59.18/9.57
Packed density/kg·m^{-3}	6860	4200
Specific heat/ J·kg^{-1}·K^{-1}	500	419
H_2 capacity/wt%	1.5	1.4
Effective thermal conductivity/W·m^{-1}·K^{-1}	–	1
Bed permeability/m^2	–	1.3×10^{-12}
Dynamic viscosity/Pa.s	8.4×10^{-6}	

Before conducting the MHT-PCM systems experiments, the intrinsic properties of the AB2-type hydride and PCM were determined using a small sample weight. Firstly, the thermo-physical parameters of coconut oil were determined by differential scanning calorimetry (DSC), using the PerkinElmer STA 8000. In doing that, the DSC of 73 mg of coconut oil at 5 °C/min was conducted. The calorimetry result is plotted in Fig. 4. The instrument software estimates that the peak area results in 97 kJ·kg^{-1} latent heat. The melting point is about 27–28 °C (peak of the DSC signal). These values are within the range reported in the literature [53]. Unfortunately, it was impossible to pinpoint the freezing point of coconut oil as our instrument does not allow cooling below 15 °C. The DSC peak was curve fitted with the rate of a sigmoid function, Eq. (8), for simulation purposes. The result showed a good fit, with a Pearson coefficient $R^2 = 0.9967$, was obtained. It is noteworthy to mention, although not within this work's scope, the DSC peak's curve fitting with other well-known peak functions (Gaussian, Rayleigh, Log-Normal distributions) also showed a good fit.

Secondly, a selected AB2-type hydride's intrinsic kinetics was determined by conducting hydrogen absorption experiments with c.a. 0.98 g. The H_2 absorption experiments were conducted using a circulating water bath pump at constant initial H_2 pressure but at different cooling temperatures. The temperature of the MH sample and the hydrogen pressure in the reference volume were monitored. Then the change in the number of hydrogen moles absorbed was calculated using Eq. (11). The curve fitting of the conversion rate (Eqs. (12) or (13)) with the experimental data allows us to determine the kinetic parameters (k_a, E_a) and the thermodynamic properties (ΔH and ΔS) simultaneously. Fig. 5 depicts the results of the fitting. Overall, there is a goodness of fit with a coefficient of determination above 0.99. The thermophysical properties of the AB2-type hydride and PCM are listed in Table 3. The most critical parameter is the activation energy, which is still in the range of previously reported values, i.e., between 20and 22 kJ·mol^{-1} [54,55]. The typical standard deviation on the k_a is high as its influence on the kinetics data is negligible.

4. Model solving and validation

The governing equations were solved in COMSOL Multiphysics 3.5a using three module applications: “chemical engineering module”, “Earth Science Module” and the “PDE, coefficient Form”. The following settings were chosen: a time stepping using backward Euler discretization with a default time step of 10^{-2}; Absolute tolerance of 10^{-4}; a linear system solver PARDISO (parallel direct solver). It should be noted that COMSOL has several linear system solvers that can be tested depending on the problem. We have solved our model using UMFPACK (Unsymmetric MultiFrontal Package), SPOOLES (SParse Object Oriented Linear Equations Solver), and PARDISO. The result showed that PARDISO is the best solver regarding solution time. More details about selecting a linear

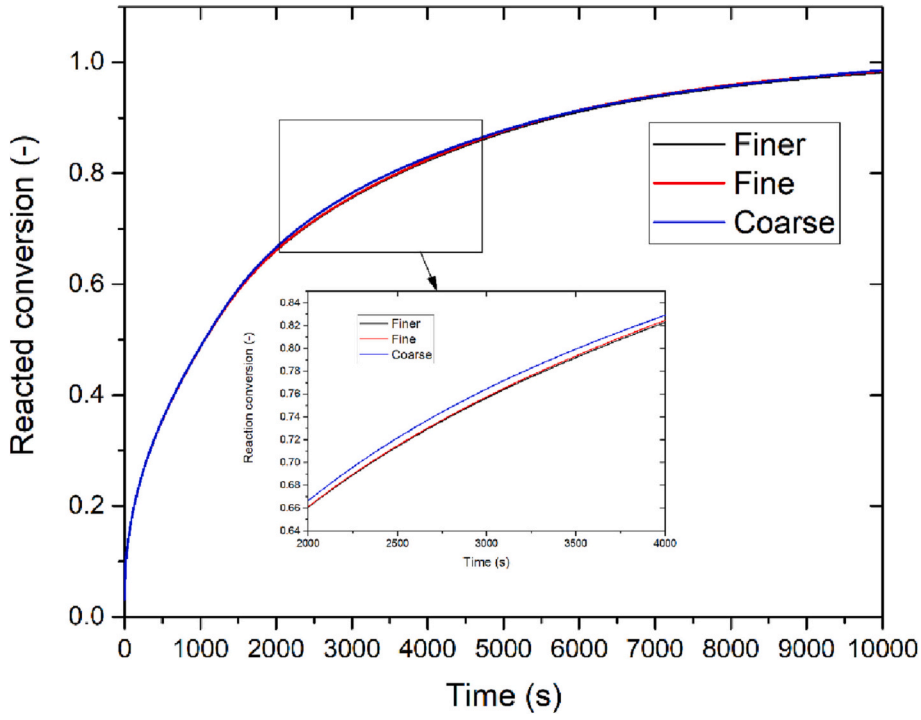

Fig. 6. Grid independence test.

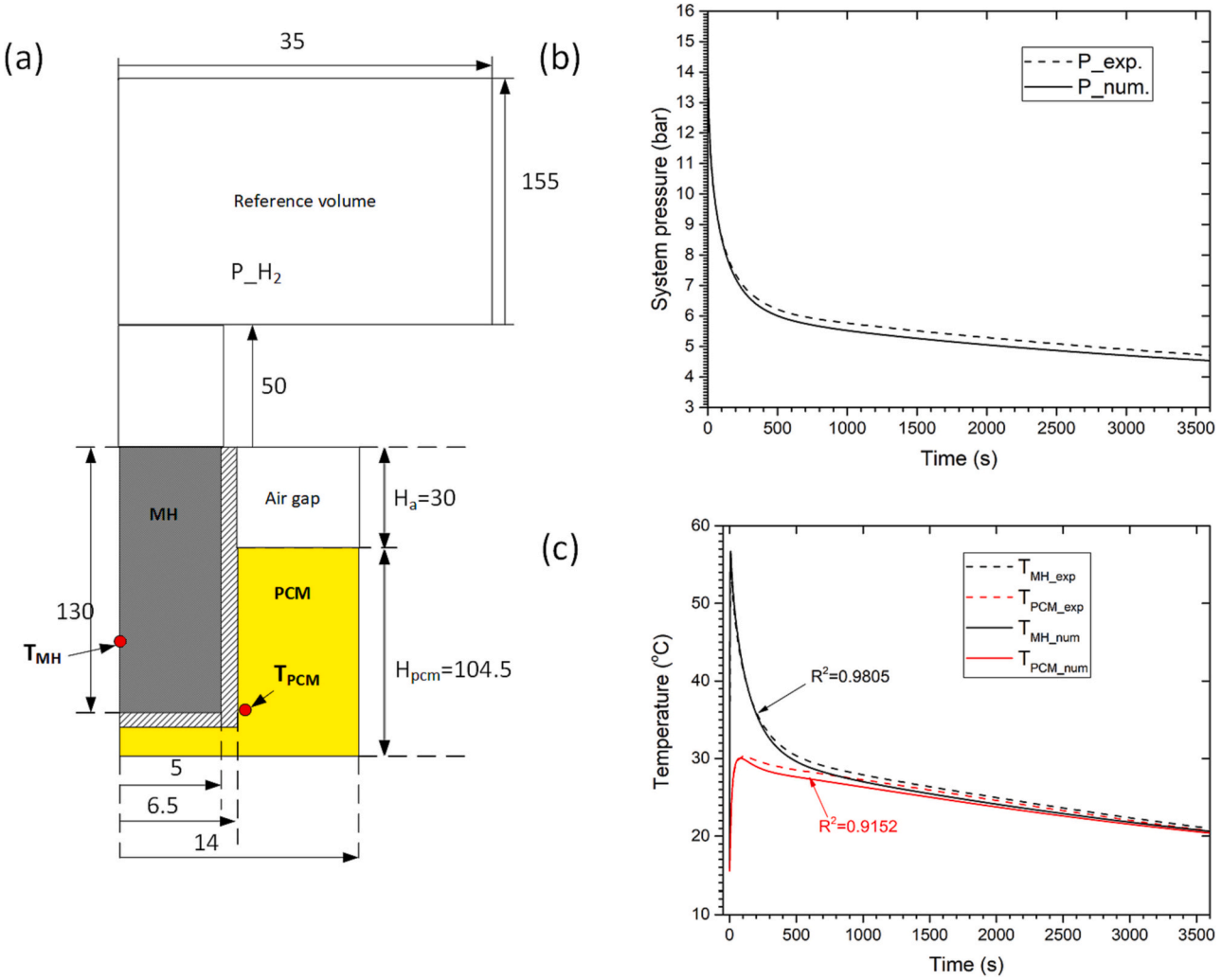

Fig. 7. Model comparison with the experimental data: (a) computational volume, (b) change in hydrogen pressure in the reference volume, (c), temperature change in the AB2-type hydride MH and PCM domain.

system solver can be found online in a "COMSOL Multiphysics reference guide". The thermophysical properties of the hydride materials (AB2 and AB5 types) for model validation, solving, and optimization are displayed in Table 3. Several mesh sizes from coarse (5132 elements), and fine (6478) to finer (7244) were tested to ensure accuracy on the calculated hydrogen charging/discharging times. Fig. 6 shows the results of the mesh independence test. The error on the reacted fraction using fine and finer meshes was <0.1 %. Therefore, a fine mesh was chosen for the rest of the calculations to balance accuracy and computational time. One single-point simulation with fine mesh took approximately 52 min on our computer: DELL XPS Intel i7-8700 hexacore (12 threads) CPU @3.20GHz with ~32 GB of RAM.

Fig. 7a depicts the computational volume of a Sievert-type experiment. It consists of three domains, the H_2 gas, the MH, and the PCM. The dimension of the H_2 gas domain is calculated in a way that its volume matches 604 cm^3. The coordinates of the K-type thermocouples monitoring the temperature inside the MH and PCM are as follows; T_{MH} ($r = 0$; $z = 20 \pm 1$ mm), T_{PCM} ($r = 7 \pm 1$ mm; $z = 5 \pm 2$ mm). Fig. 7b compares the experimental change of H_2 pressure and the numerical model. The model agrees well with the experimental data up to 200 s; then under-predicts the H_2 pressure by ~0.3 bar max. Fig. 7c shows the comparison of experimental data and numerical model for the temperatures of MH and PCM. The Pearson correlation coefficient R^2 assesses the error between the observed and simulation data. As can be seen from the figure, $R^2 = 0.98$ shows a good correspondence between experimental data and the numerical model for T_{MH} with a confidence level above 98 % (i.e., error within 1-$R^2 = \pm 2$ %). However, the model did not predict the PCM's temperature well, with an error above ±8 % ($R^2 = 0.91$). This great error might be ascribed to the uncertainty of the coordinates of T_{PCM}, since the thermocouple was manually placed in the PCM jacket and could be subjected to vibrations during the measurements. Other possible sources of errors could be the uncertainty on the measured thermophysical properties of coconut oil.

5. Results and discussion

5.1. Sensitivity analysis

The first step in this analysis is to determine the effects of the thermophysical properties of the reference PCM on the H_2 charging/discharging times into the metal hydride. This is achieved by evaluating the g_X factor for each parameter. Fig. 8 shows the parametric study of PCM's intrinsic properties on the H_2 charging/discharging times. As can be seen, the increase of the mushy (phase transition) zone by 10 % (i.e., from 1 to 1.1 K) has a subtle effect on the t_{ch} and t_{dis}, which decrease by 0.4 and 0.5 %, respectively. Since the melting point influences the heat transfer by conduction, as explained in Fig. 2, the melting point increase from 35 to 38 °C augments the hydrogen charging time by 2.12 % while shortening the discharging time by 5.71 %.

On the other hand, the parameters contributing to the thermal

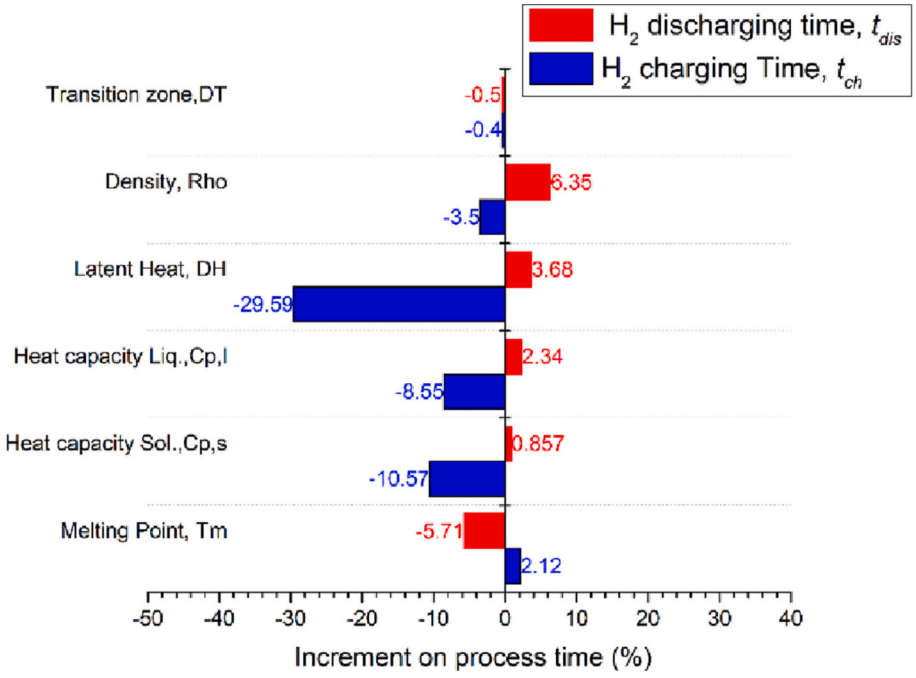

Fig. 8. The effect of the thermophysical parameters of RT35 on the hydrogen charging time, t_{ch}/discharging time, t_{dis}: Each parameter is increases by 10 % from the properties of the reference PCM (RT35)

capacity of the system (density, latent heat, and heat capacity) drastically impact the H_2 charging time. For example, increasing the latent heat by 10 % reduces the H_2 charging time by 29.59 %. Therefore, combining these three parameters would limit the temperature increase during an exothermic reaction (hydriding process), thereby promoting a fast hydrogen charging process (short t_{ch}). At the same time, their effect on the hydrogen discharging process would be reversed (prolonged t_{dis}).

5.1.1. Effect of the melting point

Fig. 9 shows the effect of the melting point on the H absorption/desorption. As the melting point of a PCM decreases under given operating pressure of 10 bar and 1.5 bar H_2 ab/desorption, respectively, the H_2 absorption time increases, whereas the desorption time decrease. As explained before, it is due to the temperature gradient between the PCM and the MH, which is the driving force of the heat transfer by conduction. However, though there is a monotonic trend of the PCM melting point on either H absorption or desorption time, it is possible to find an optimum melting point at which the overall process time (absorption and desorption) is minimum. It can be observed the blue line on the graph is convex, which means that a minimum exists. Therefore, a melting point of 41.96 °C is optimum for this H_2 storage process. This value coincidentally agrees with the one given in the study by Jing Yao et al. [25], which found a melting point of 42 °C. Overall, given the operating conditions of the hydrogen storage system, a PCM melting point at around 42 °C ($\beta = 0.55$) is optimal.

5.1.2. Effect of the PCM hysteresis or subcooling on the H_2 sorption time

For any PCM, it is experimentally observed that the melting temperature differs from the freezing (solidification) one. More specifically, the freezing process occurs at a temperature below the melting point. This phenomenon is known as sub-cooling and can affect the performance of the energy storage of the PCM. Fig. 10 shows that the increase in the sub-cooling effect slows down the H_2 desorption process as the driving force of the heat transfer decreases considerably. For example, increasing the sub-cooling from 0.5 to 1 °C, the hydrogen desorption rises from 5603 to 5650 s, which is less than a minute delay. However, by increasing the subcooling to 5 °C, the H_2 desorption is delayed for a further ~7 min (422 s). Furthermore, doubling the sub-cooling to 10 °C shows that the delay in H_2 desorption increases by 19 min. These results show that the selection of PCM with a negligible or small sub-cooling should be done to keep the hydrogen desorption time at a minimum.

5.1.3. Effect of the latent heat of fusion

Under a given PCM reactor size, the variation of the PCM latent heat affects the total thermal energy available for the heat dissipation/absorption during the H_2 absorption/desorption process, respectively. It is seen from Fig. 11a that by increasing the latent heat, the H_2 absorption time decreases from 9880 s (120 kJ·kg^{-1}) to 2732 s (250 kJ·kg^{-1}). In effect, for latent heat in the range of 120–165 kJ·kg^{-1}, the PCM absorbs part of the H_2 absorption heat, and the remainder is stored as sensible heat, which limits the hydrogen absorption effectiveness. The figure shows that the maximum H_2 reacted fraction is specified in the range of 0.67–0.9. Therefore, the selection of PCM with latent heat above 150 kJ/kg leads to a better hydrogen sorption performance, with a reacted fraction reaching 1.

On the other hand, from the figure, it is seen that the H_2 desorption follows a reverse trendline as t_{dis} is relatively fast for the given range of latent heat. The hydrogen desorption rapidly increases from 3307 s to 6246 s (165 kJ·kg^{-1}) and gradually increases beyond 200 kJ·kg^{-1}. A simple explanation of this behavior during the H_2 desorption is that the temperature gradient is higher as lower latent heat is concerned.

5.1.4. Effect of the PCM density and heat capacity (volumetric thermal capacity)

Physically speaking, the temperature of materials with high thermal capacity slowly increases when absorbing heat by thermal diffusion (note that the thermal diffusivity is inversely proportional to the volumetric heat capacity: $\lambda/(\rho C_p)$). Fig. 11b sketches the impact of PCM's volumetric heat capacity on the H_2 ab/desorption times when the latent heat is kept fixed. The PCM temperature increases rapidly for a low thermal capacity of 1 MJ·m^{-3}·K^{-1}. As a result, the difference between the MH and PCM temperature decreases (the driving force of conductive heat), which leads to a prolonged hydrogen absorption time of 9000 s. As we select PCM with high thermal capacity beyond 2 MJ·m^{-3}·K^{-1}, it is seen that the H_2 charging time drastically reduces by more than a half, i.e., 4450 s.

Interestingly, this graph allows the ranking of different practical PCMs based on their thermal capacity. It is seen that the selection of paraffin with low thermal capacity ranging between 1 and 2 $MJ{\cdot}m^{-3}{\cdot}K^{-1}$ for hydrogen storage applications will lead to relatively high cumulative H_2 charging/discharging times (t_{ch} + t_{dis}) around 13,000–11,000 s. For other types of PCMs (salt hydrates and eutectic) where the thermal capacity is beyond 2 $MJ{\cdot}m^{-3}{\cdot}K^{-1}$, t_{ch} gently declines from 3200 to 2700 while t_{dis} increases from ~7200 to 8100 s. Nevertheless, the cumulative process time only marginally varies (4.15 % increase). These two parameters contribute significantly to the sensible heat (Stefan number). As can be seen from Fig. 11b, increasing the density or heat capacity at constant latent heat, the H_2 charging time decreases.

5.1.5. Effect of fin geometric parameters on the H_2 ab/desorption time

The effects of fin thickness, length, spacing, and aspect ratio on the H_2 absorption/desorption times are portrayed in Fig. 12. Fig. 12a shows the behavior of the process times with the fin thickness. From the figure, the absorption time increases for higher thicknesses while an opposite trend is observed for the H_2 desorption time. Although increasing fin thickness increases the thermal conductivity (heat transfer phenomenon), the maximum hydrogen absorbed decreases as a result of the replacement of active PCM material by passive fins. One can see the maximum capacity decrease from 100 % to 82.11 % for a fin volume fraction hike from 9 to 51.83 %. On the other hand, Fig. 12b shows an interesting behavior. The increase of the fin length at a fixed thickness of 2 mm does not critically affect the amount of PCM in the jacket as the fin volume fraction increases by 9–22 %. Therefore, the maximum H_2 storage capacity is 100 % regardless of the fin volume fraction.

Furthermore, the H_2 charging time displays a convex behavior regarding the fin length (a downward trend, then an upward one). As a result, there is a fin length (~17 mm) whereby the H_2 charging time (t_{ch}) is minimum. However, owing to the monotonic decrease of the discharging time with length, the optimum fin length is located at 19–20 mm for a minimum overall process time ($t_{ch} + t_{dis}$). Fig. 12c portrays the fin aspect ratio (AR) effect on the H_2 charging/discharging time. The AR is the ratio of fin length to thickness at a constant fin volume fraction of 19.17 %. As can be seen at fixed fin volume fraction, the performance indicators (t_{ch}, t_{dis}, and $t_{ch} + t_{dis}$) decrease with the increase of fin AR. Based on the variation range of the AR, t_{ch}, t_{dis}, and $t_{ch} + t_{dis}$ vary by 11.75, 10.71 and 11.19 %, respectively. The corresponding fin length and thickness values for the given AR are tabulated in Table 4. Fig. 12d depicts the effect of fin spacing (FS) on tch and t_{dis}. It is observed that, for small FS, there is an imbalance of fin distribution inside the PCM jacket as the fins are localized in the middle of the jacket (lengthwise). As a result, the top and bottom parts of the PCM jacket experience poor heat transfer conditions because of the low thermal conductivity. This leads to prolonged H_2 charging/discharging times, e.g., for FS = 5 mm, t_{ch} = 13,550 s, and t_{dis} = 14,940 s. Increasing the FS to 8 mm considerably reduces the process times t_{ch}, and t_{dis} by 24.54 and 32.19 %, respectively.

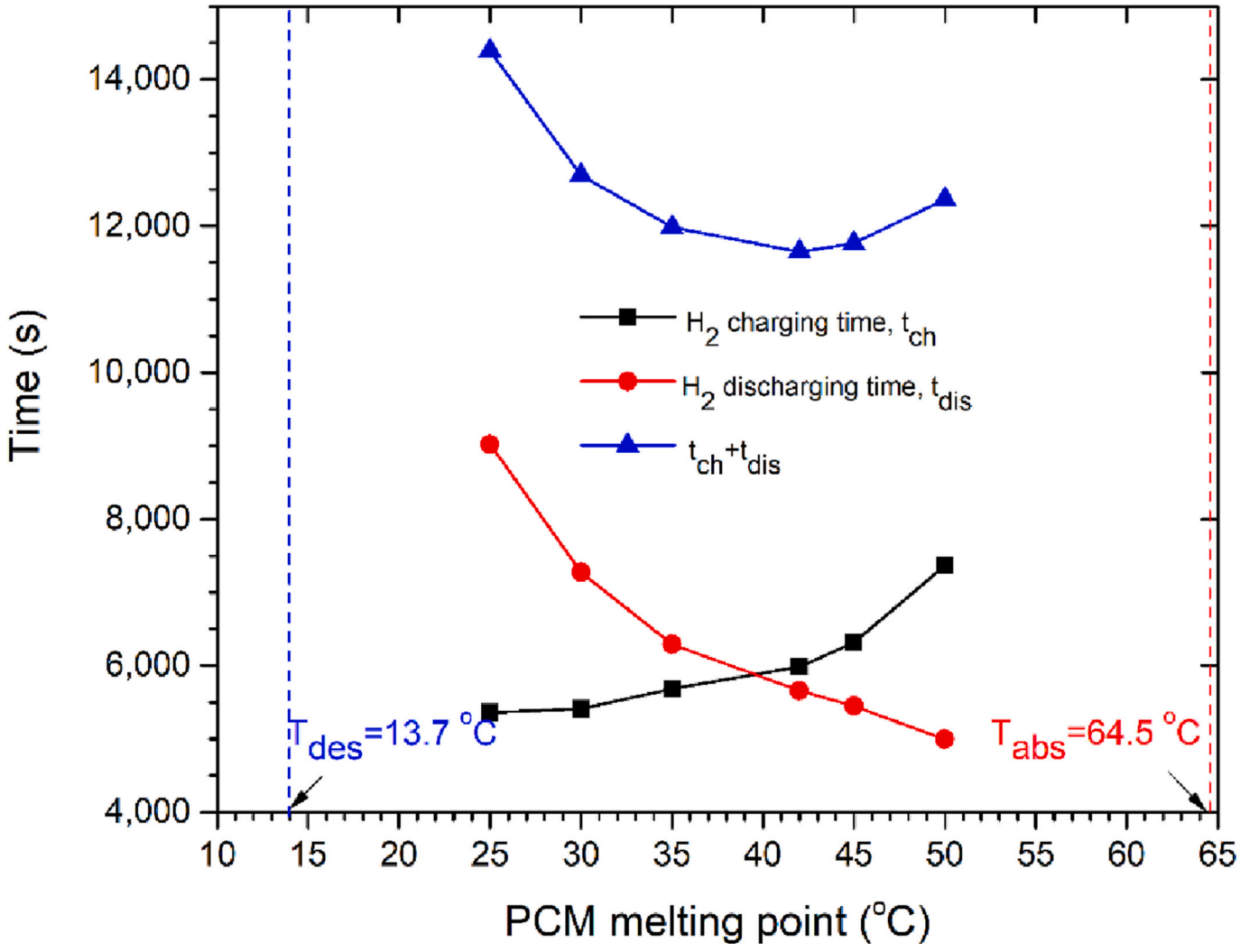

Fig. 9. The effect of PCM melting point on the hydrogen charging/discharging times.

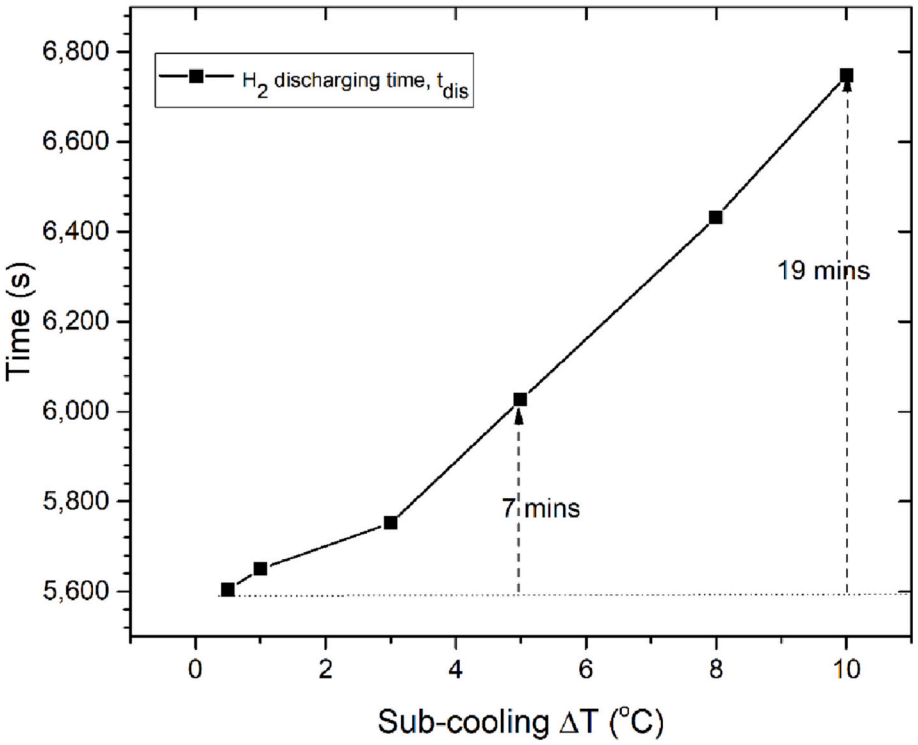

Fig. 10. The effect of hysteresis on the hydrogen discharging time.

It is seen from Fig. 12d that t_{ch} and t_{dis} are minimum with FS = 10 mm, as the fins are well distributed in the PCM jacket. Therefore, the increase of FS from 8 to 10 mm results in a reduction of t_{ch} and t_{dis} by 45.85 and 36.50 %, respectively.

5.2. Multi-objective optimization procedure and results

5.2.1. Optimization formulation

The sensitivity analysis results showed that the hydrogen charging/discharging times evolve in opposite trendlines for most of the decision variables, i.e., in a conflicting manner. This contradictory behavior gives rise to multi-objective optimization. For example, hydrogen storage applications aim to decrease the storage and utilization (restore) process time. On the other hand, in MHT-PCM systems, H_2 charging time can be longer and is not as crucial as in mobile applications where a charging time of a maximum of 5 min is required [3]. However, the H_2 discharging time is primordial as it dictates the H_2 supply flow rate to a given fuel cell device. Therefore, short H_2 discharging times translate to the utilization of high-power fuel cells. Overall, an optimization problem that simultaneously minimizes the H_2 charging and discharging time can be reasonably formulated for this type of application.

Furthermore, since increasing the volume of the fin would improve the PCM thermal conductivity at the expense of decreasing the volume of PCM (volumetric energy density), it is judicious to constrain the fin volume fraction to that of PCM to a value of 20–30 %. Note that the definition of this constraint is subjective and depends on the designer's discretion. However, given this discussion mentioned above, the objective problem is defined as follows:

$$\begin{cases} minimize\ (t_{ch}, t_{dis}) \\ s.t. V_{fin} \leq 0.3 \times V_{pcm} \end{cases} \quad (25)$$

The optimization variables include nine parameters, of which six are the PCM thermophysical properties (T_m; ΔH_{pcm}; ρ_{pcm}; $C_{p,l}$; $C_{p,s}$; ΔT) and three are the fin parameters (length, thickness, and fin spacings). The upper and lower bounds of these parameters are given in Table 5. The PCM properties range includes all types of low-temperature PCM (organic paraffin, salt hydrates and eutectic).

The problem was solved in MATLAB platform using the multi-objective optimization genetic algorithm NSGA-II, which was also provided in our previous work [48]. The genetic algorithm method was selected with a population of 30 individuals from each generation. Note that the selection of the number of individuals is the balance between computation time (Finite element or volume simulation for the evaluation of an individual) and a clear Pareto front, i.e., the curve fitting of the Pareto front becomes difficult with only few individuals (less or equal than 10). Therefore, the choice of 30 individuals was made to quicken the obtainment of the final Pareto front as one individual's simulation and evaluation time was above 50 min on our personal computer. The crossover and mutation probabilities were 80 % and 5 %, respectively, and the number of generations adopted was 100.

5.2.2. Optimization results

Fig. 13 sketches the Pareto front of optimal solutions. Under the studied range of decision variables, the discharging time decreases as the charging time increases. However, it is seen that by removing the two endpoints of the Pareto front (results of single-objective optimization), the front decreases at a slow rate, i.e., for an increase in t_{ch} from 2370 to 8807 s, the discharging time decreases only in the range 8530 to 4988 s. To better understand the effects of the decision variables on the objective functions, six (6) solutions are selected for the discussion (highlighted in red on the graph). Note that there is no standard method for selecting optimal solutions on the Pareto front. Nonetheless, we have selected these six solutions in such a way that they are well spread on the Pareto frontier. Furthermore, the design parameters alongside the obtained objectives are tabulated in Table 6.

Solutions #1 and #6 are the results of MHT-PCM designs with minimum H_2 charging and discharging time, respectively. These solutions are obtained for constrained single-objective optimization problems. Looking at these design parameters, one can see that the melting point is the most impactful parameter due to its effect on the heat conduction driving force (as discussed above). Therefore, the melting point for these optimal solutions (#1, 6) converges towards the lower

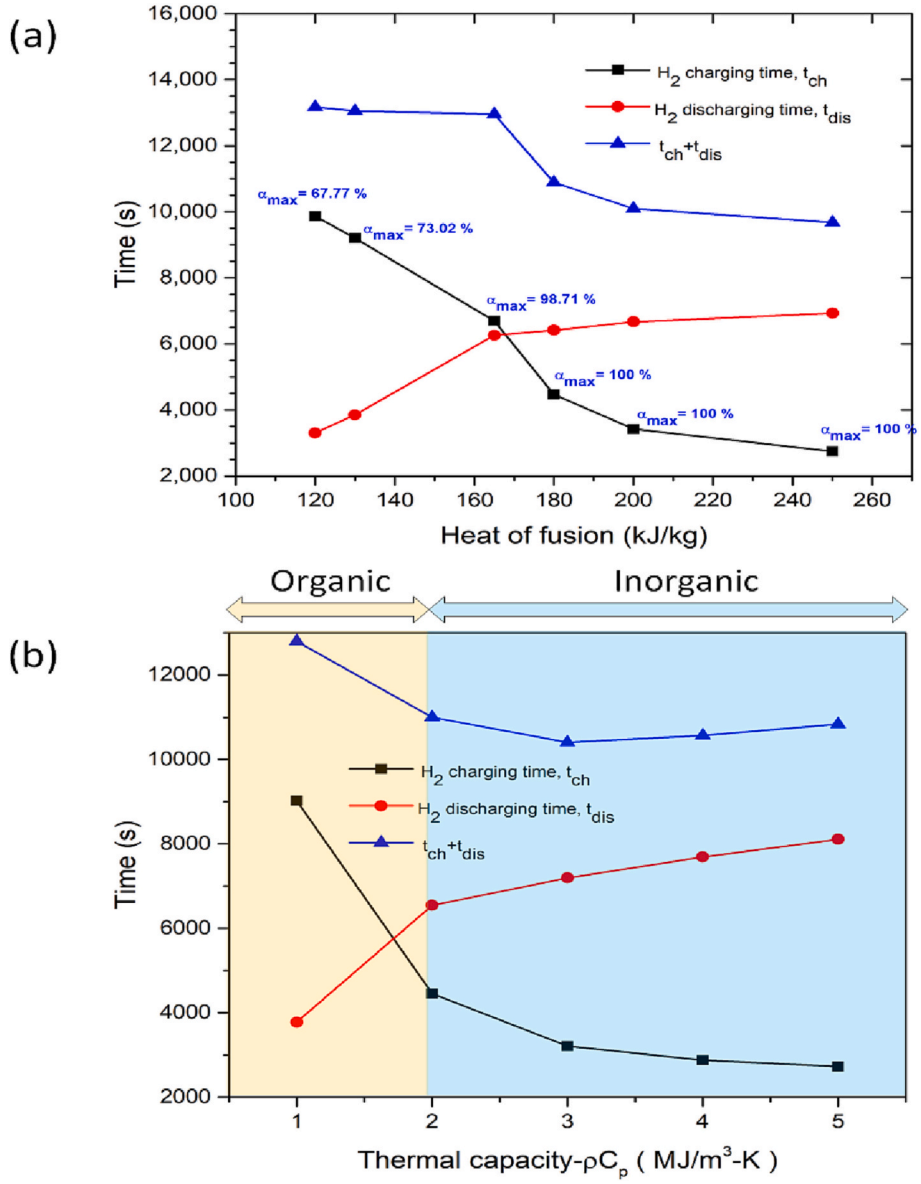

Fig. 11. The effects of apparent heat capacity on the hydrogen charging/discharging times: (a) the effect of latent heat, (b) the effect of the volumetric thermal capacity.

and upper bound of the temperature range, respectively. In addition, regardless of the optimal solution, PCM's specific heat and latent heat should point to a narrow range of 2000/3000 J/kg K and 200–216 kJ·kg^{-1}, respectively.

On the one hand, the transition temperature is spread on a wide range of 0.5–4 °C. This is because it was shown during the sensitivity analysis that it does not significantly influence the objectives. On the other hand, the PCM density for optimal PCMs falls within two ranges <1000 kg·m^{-3} (paraffin) and over 1000 kg·m^{-3} (salt hydrate and others).

For practical applications, one should select a single solution among the optimal solutions given in the Pareto front. This solution selection is subjective as it depends on the decision-maker. Several decision-making tools, e.g., LINMAP, TOPSIS, and fuzzy approach, gives a final solution utterly different from each other [56]. In this work, the LINMAP (Linear Programing for Multidimensional Analysis of Preference) [57] is adopted to find the best optimal solution among the Pareto front. It measures the distance (Euclidian) between the ideal solution and the solutions located on the Pareto front. The Euclidian distance is given by the equation below [56,57]:

$$\Delta_i = \sqrt{\sum_{j=1}^{n} w_j \left(F_{i,j} - F_{j,ideal}\right)^2} \tag{26}$$

where, i is the index of solution points on the Pareto front, j is the objective index in the objective space of n dimensions ($n = 2$ in this work), w_j is the weight factor or the importance of the objective F_j. $F_{j.ideal}$is the minimum/maximum objective function in the objective space depending on a single objective minimization/maximization problem, respectively. Before the distance calculation, the objectives should be scaled if their order of magnitude is different. However, for our problem at hand, the two goals are from the same unit and are equally important. Therefore, the weight factor is set to 1 ($w_1 = w_2 = 1$), and scaling is not required. The distance between all the selected solutions on the Pareto front and the ideal solution is calculated. As can be seen from Table 6, Solution #2 on the graph has the shortest distance of 4811 s from the ideal solution (note that the distance to the ideal solution of all 30 optimal solutions on the Pareto front was calculated and

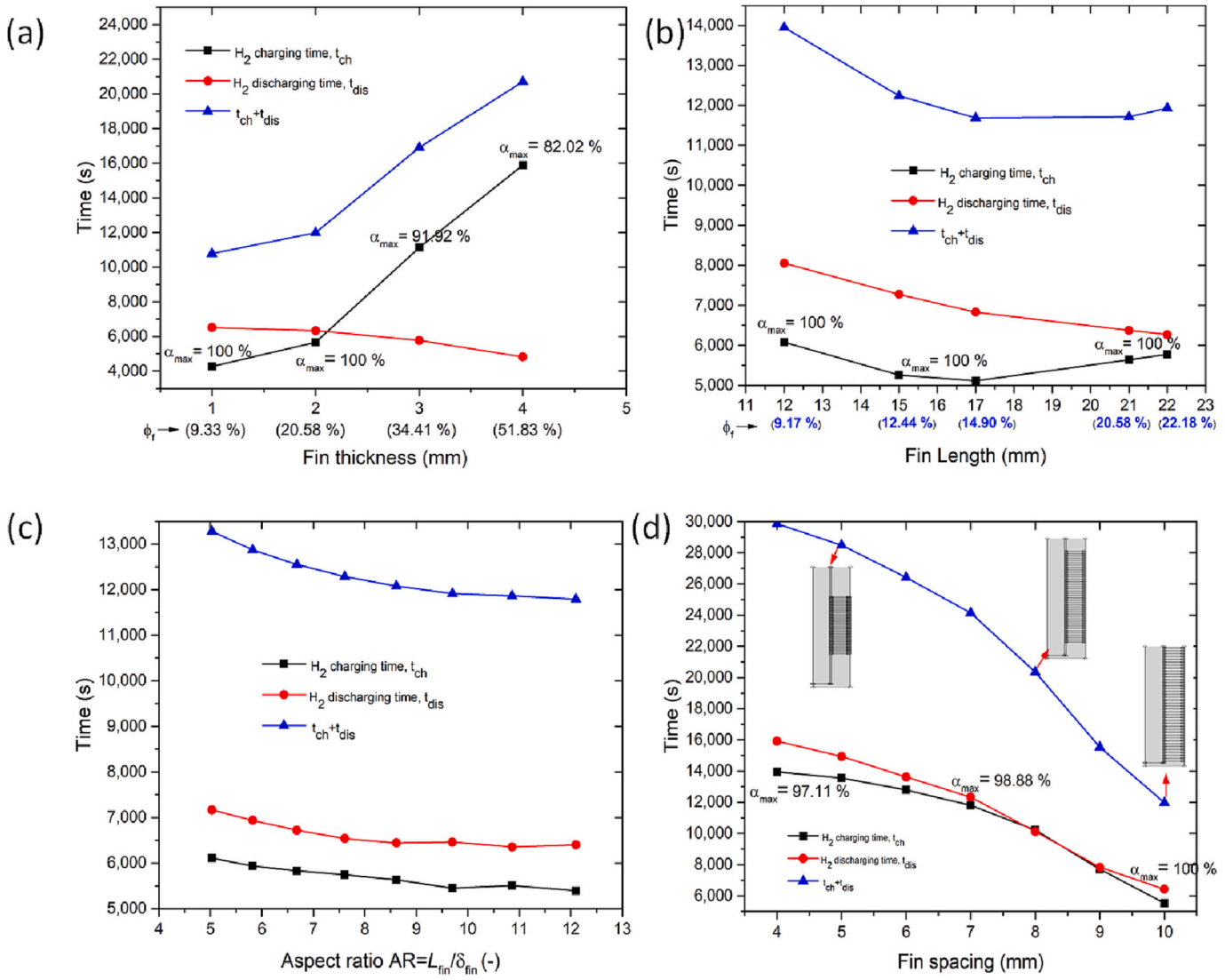

Fig. 12. The effects of the fin geometric parameters on hydrogen charging/discharging times: (a) fin thickness, (b) fin length, (c) fin aspect ratio at a fixed volume fraction of 19.76 %, (d) fin spacing.

Table 4
The effect of fin size on the performance indicators at fixed fin volume fraction, $\phi_f = 19.76$ %.

L_{fin} (mm)	δ_{fin} (mm)	AR (−)	t_{ch} (s)	t_{dis} (s)
15	3	5.03	6110	7168
16	2.7	5.82	5936	6938
17	2.5	6.68	5832	6720
18	2.4	7.61	5746	6540
19	2.2	8.61	5636	6442
20	2.1	9.70	5452	6460
21	1.9	10.86	5510	6354
22	1.8	12.10	5392	6400

Table 5
Range of the design parameters used in the optimization process.

	Range
Melting point range T_m/°C	25–62
Mushy zone ΔT_{tr}/°C	0.5–20
Density: solid-liquid/kg·m^{-3}	760–2000
Specific heat, C_p/J·kg^{-1}·K^{-1}	1200–3000
Latent heat of fusion, ΔH_{pcm}/kJ·kg^{-1}	110–230
Fin length, L_f/m	0.01–0.022
Fin thickness, δ_f/m	0.001–0.004
Fin spacing, FS/m	0.005–0.01

solution #2 is the best optimal solution). Besides, the features of solution #2 are highlighted in bold in Table 6.

Another sensitivity analysis is performed on the selected optimal design point (solution #2) to see whether or not this design point can be further optimized. The design parameters are varied one at the time while keeping the others fixed around the optimal design parameter of design point #2. Fig. 14 exhibits the effects of the eight design parameters on the objective functions (t_{ch}, t_{dis}). Fig. 14a shows the effect of varying the PCM melting point on the objective functions. As can be seen, by increasing the melting point, the H_2 charging time increases while the H_2 discharging time shrinks. Therefore, the PCM melting causes a tradeoff between the objective functions. Nevertheless, the design point #2 (in the blue dashed box) is still optimal with the optimum melting point of 42.6 °C. In Fig. 14b, by changing the PCM density, t_{ch} decreases monotonically while t_{dis} decreases then increases with the minimum around 1107 kg·m^{-3}. Therefore for this above case, design point #2 is confirmed to be the optimum one. By increasing the latent heat, both t_{ch} and t_{dis} unidirectionally decline (Fig. 14c). Therefore this parameter does not cause a conflict between the two objective functions.

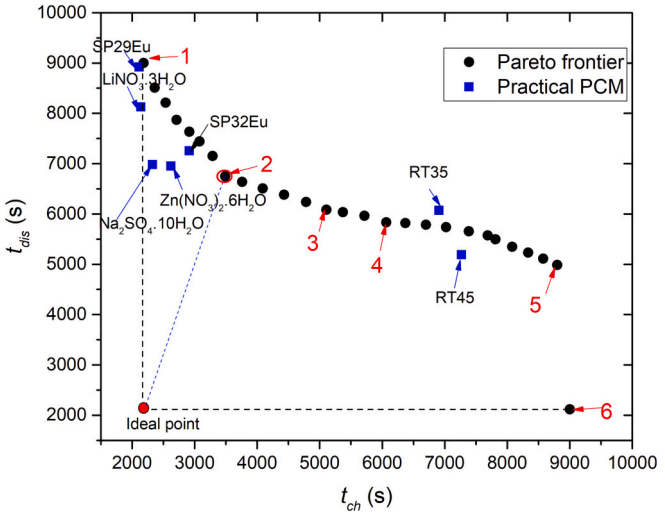

Fig. 13. Pareto front obtained after 100 iterations, the performance of practical PCMs is added to the graph (blue symbols). (For interpretation of the references to colour in this figure legend, the reader is referred to the web version of this article.)

However, it should be noted that beyond the optimum latent heat of 214 kJ·kg^{-1}, the objective functions shrink insignificantly. As a result, the selection of PCM with very high latent heat above 210 kJ·kg^{-1} for practical applications should also consider its market value. The effect of the specific heat of PCM on t_{ch} and t_{dis} is negligible as it can be seen in Fig. 14d. Fig. 14e shows the variation of objective functions with the phase transition zone, ΔT_{tr}. In effect, the increase of ΔT_{tr} influences mostly t_{dis} than it does on t_{ch}. The variation of fin length and thickness on the objective functions are plotted in Fig. 14f and g, respectively. Their change predominantly affects the H_2 discharging time, as t_{dis} decreases and then increases (convex trend) as the fin length and thickness increase. Therefore, from these figures, design point #2 with the following fin thickness of 3.53 mm and length of 18.98 mm is still the best optimum one as $t_{ch} + t_{dis}$ is the minimum. Finally, by varying the fin spacing, both t_{ch} and t_{dis} decrease simultaneously (Fig. 14h). However, changing the fin spacing from 9.53 to 10 mm causes a deviation in t_{ch} and t_{dis} of <1.8 %.

To further assess the benefits of optimizing the MHT-PCM system, the performance comparison between the MHT-PCM using the optimized design parameters of design point #2 on the Pareto front and the reference case (RT35) is conducted. Fig. 15 exhibits the transient profile of H_2 absorption/desorption of the two systems. As can be seen from the figure, the MHT-PCM using the optimized PCM has the fastest hydrogen charging/discharging time to reach 90 % of the maximum hydrogen capacity than the system using the reference PCM (RT35). Indeed, the H_2 charging time decreases by 48.69 %. Conversely, there is not so much improvement on the H_2 discharging time as the decline is only <4 %. Moreover, it is seen that using the optimized design, the maximum hydrogen capacity in the system improves from 96 % to 100 %.

One of the main limitations of the optimization procedure is that the optimal solutions obtained can be non-physical or unrealistic. For example, given the thermophysical properties of PCMs for optimal solutions, it still might be difficult to classify them or find them available on the market. Therefore, we have plotted the charging and discharging times of MHT-PCM systems using practical PCMs given in Table 2. The results of these calculations are given in blue square symbols in the Pareto front. As one can see, the salt hydrates and eutectics lead to short H_2 charging times (usually ~2000 s) but a high H_2 discharging time (~8000 s). On the other hand, paraffin waxes have a more balanced charging/discharging time. Because our Pareto front describes a minimization problem, any point below it is in an optimal region. Hence, all the practical PCMs except RT35 are optimal solutions and can be selected for MHT-PCMs systems.

6. Conclusions

Using phase change materials (PCM) in solid-state hydrogen storage applications is a promising hydride material heat storage/recovery option. However, the time for heat storage/recovery storage depends on multiple factors, such as the reactor design and the intrinsic properties of the selected PCM. This work presented a methodology for minimizing the H_2 absorption/desorption times in a $LaNi_5$-based MHT-PCM systems using finite element analysis and multi-objective optimization. The main results are summarized as follows:

- The numerical model was validated with in-house experiments using coconut oil as PCM. The results show a qualitative and quantitative agreement with the experiments at minimum errors of <10 %.
- Sensitivity analysis using a gradient-based procedure showed that the latent heat and the specific heat capacity have a significant effect (reducing the charging time by up to 29 %) on the H_2 absorption time. Furthermore, selecting the melting point is crucial in improving the heat transfer between the PCM and metal hydride.
- The subcooling property of PCM should be considered in practical applications as it only has a deleterious effect on the hydrogen desorption time. In this given case, the subcooling of about 5 °C can delay the hydrogen desorption time by 7 min compared to the case whereby it is not accounted for (no subcooling).
- A combination of finite element simulation with a genetic algorithm is used to determine the Pareto front of minimizing at the same time the H_2 charging/discharging times in the H_2 storage system. Then 6 points (#1 to #6) on the Pareto front were selected for discussing their features. The two endpoints (#1 and #6) of the Pareto front are optimal solutions in a single objective optimization. On the other hand, using a simple decision-making tool (LINMAP technique), point #2 on the Pareto front is the best among the optimal points.
- The optimal design reduced the hydrogen ab/desorption times by 48.6 % and 4 % of the reference MHT-PCM design. At the same time,

Table 6
Selected optimal solutions and their corresponding design variables: solution #2 is selected using the LINMAP decision-making approach.

	1	6	5	3	2	4	Ideal solution
T_m (°C)	25	62	56.2	49.15	**42.65**	51.80	–
Cp_s/Cp_l (J·kg^{-1}·K^{-1})	2047/3011	1959/2916.9	1958/2917	1946/2858	**1964/2878**	1958/2877	–
ΔH_{pcm} (kJ·kg^{-1})	216.12	199.56	201.47	216.60	**214.65**	217.29	–
ρ_{pcm}(kg·m^{-3})	1136	770	788	800	**1107.62**	798.94	–
ΔT_{tr} (°C)	3.93	0.5	1.09	1.81	**0.5**	1.2	–
L_{fin} (mm)	19.09	18.60	18.71	18.90	**18.98**	18.44	–
δ_{fin} (mm)	3.53	3.28	2.81	3.01	**3.53**	2.69	–
FS (mm)	9.6	9.21	9.45	9.47	**9.33**	9.33	–
t_{ch} (s)	2186	>9000	8802	5108	**3488**	6064	2186
t_{dis} (s)	>9000	2116	4986	6084	**6748**	5836	2116
Δ (s)	6884	6814	7211.68	4927.78	**4811.50**	5376.76	0

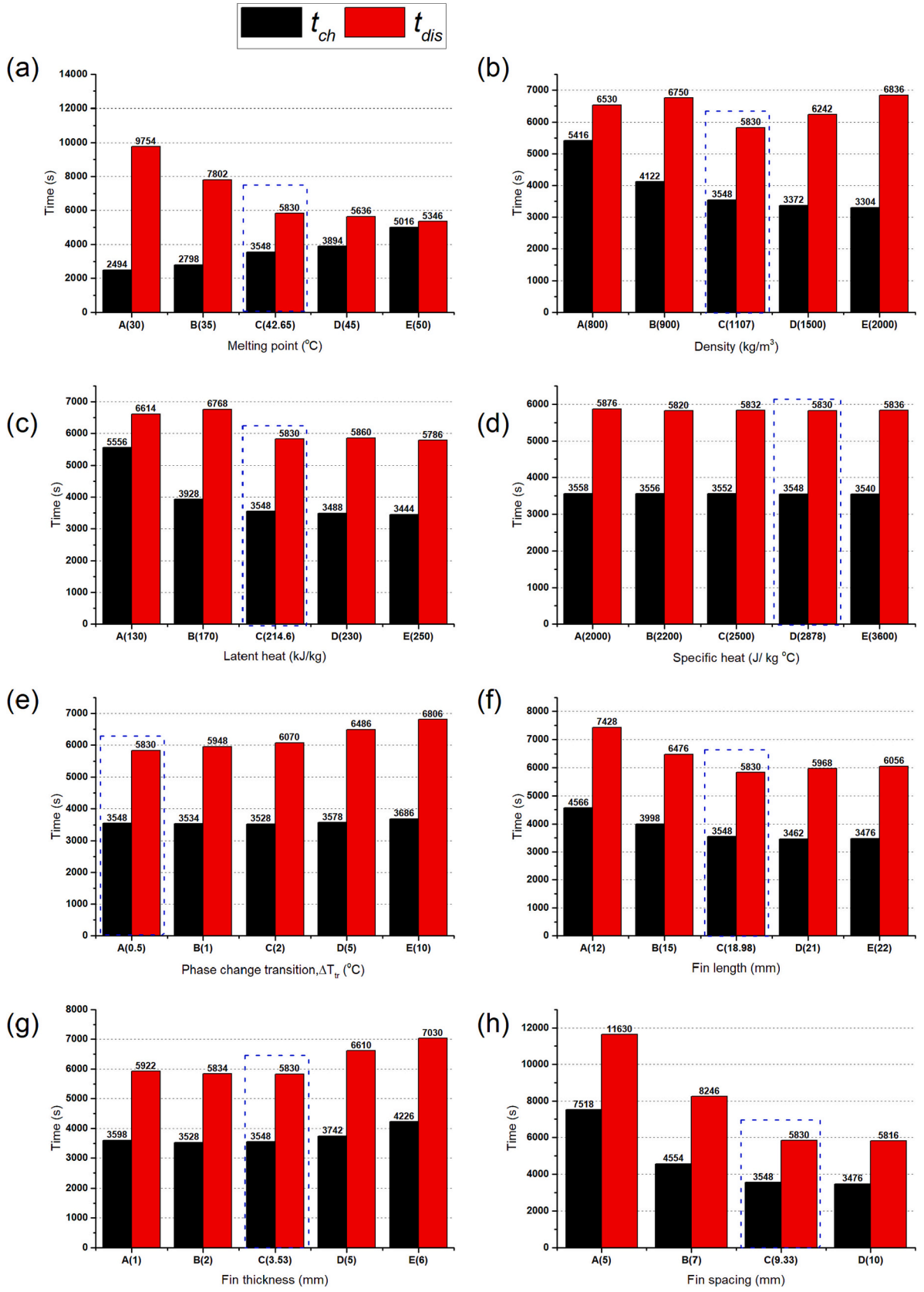

Fig. 14. The effects of design parameters on the objective functions (t_{ch} and t_{dis}) with optimal solution #2 taken as the reference point: a) melting point, b) density, c) latent heat, d) specific heat, e) phase change transition, f) fin length, g) fin thickness, h) fin spacing. (For interpretation of the references to colour in this figure, the reader is referred to the web version of this article.)

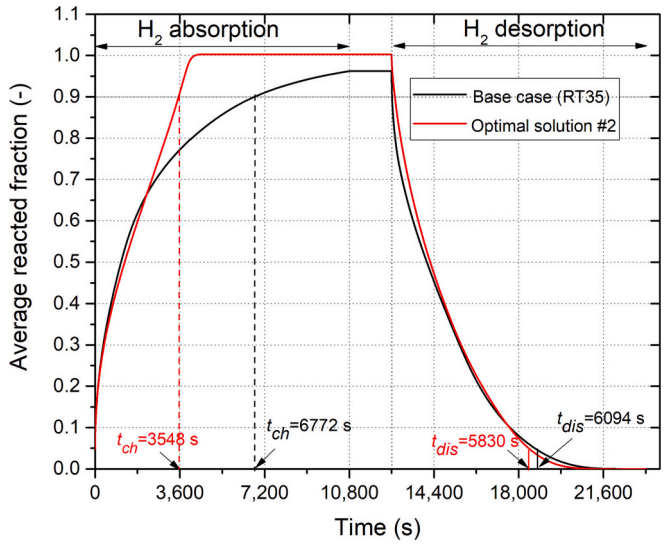

Fig. 15. Comparison of hydrogen storage performance between the reference and optimized MHT-PCM systems.

the hydrogen storage efficiency of the optimal design is 100 % as compared to 96 % for the reference design.

CRediT authorship contribution statement

Serge Nyallang Nyamsi: Conceptualization, Methodology, Formal analysis, Software, Writing – original draft, Visualization. **Ivan Tolj:** Conceptualization, Writing – review & editing, Supervision, Project administration, Funding acquisition. **Sivakumar Pasupathi:** Project administration, Funding acquisition, Supervision.

Declaration of competing interest

The authors declare that they have no known competing financial interests or personal relationships that could have appeared to influence the work reported in this paper.

Data availability

Data will be made available on request.

Acknowledgments

This work is funded by the South Africa Department of Science and Innovation (DSI) within the HYSA program (project KP6-S01). The international collaboration is supported by the EC, Grant Agreement number: 778307-HYDRIDE4MOBILITY – H2020-MSCA-RISE-2017, and supported by the Virtual Telemedicine Assistance - VITA, a project co-financed by the Croatian Government and the European Union through the European Regional Development Fund - the Competitiveness and Cohesion Operational Programme (KK.01.1.1.01).

References

[1] A. Hugo, P. Rutter, S. Pistikopoulos, et al., Hydrogen infrastructure strategic planning using multi-objective optimization, Int. J. Hydrog. Energy 30 (2005) 1523–1534.
[2] A. Züttel, Materials for hydrogen storage, Mater. Today 6 (2003) 24–33.
[3] R.K. Ahluwalia, T.Q. Hua, J.K. Peng, On-board and off-board performance of hydrogen storage options for light-duty vehicles, Int. J. Hydrog. Energy 37 (2012) 2891–2910.
[4] S.N. Nyamsi, F.S. Yang, Z.X. Zhang, An optimization study on the finned tube heat exchanger used in hydride hydrogen storage system-analytical method and numerical simulation, Int. J. Hydrog. Energy 37 (2012) 16078–16092.
[5] M. Afzal, R. Mane, P. Sharma, Heat transfer techniques in metal hydride hydrogen storage: a review, Int. J. Hydrog. Energy 42 (2017) 30661–30682.
[6] J. Zhang, T.S. Fisher, P.V. Ramachandran, J.P. Gore, I. Mudawar, A review of heat transfer issues in hydrogen storage technologies, J Heat Trans–Trans ASME 127 (2005) 1391–1399.
[7] M. Nagel, Y. Komazaki, S. Suda, Effective thermal-conductivity of a metal hydride bed augmented with a copper wire-net matrix, Journal of Less-Common Metal 131 (1987) 426.
[8] F. Laurencelle, J. Goyette, Simulation of heat transfer in a metal hydride reactor with aluminium foam, Int. J. Hydrog. Energy 32 (2007) 2957–2964.
[9] S. Mellouli, H. Dhaou, F. Askri, A. Jemni, S. Ben Nasrallah, Hydrogen storage in metal hydride tanks equipped with metal foam heat exchanger, Int. J. Hydrog. Energy 34 (2009) 9393–9401.
[10] A. Chaise, P. de Rango, P. Marty, D. Fruchart, S. Miraglia, R. Olives, et al., Enhancement of hydrogen sorption in magnesium hydride using expanded natural graphite, Int. J. Hydrog. Energy 34 (2009) 8589–8596.
[11] F.A.M. Elhamshri, M. Kayfeci, Enhancement of hydrogen charging in metal hydride-based storage systems using heat pipe, Int. J. Hydrog. Energy 44 (2019) 18927–18938.
[12] C. Chung, S.-W. Yang, C.-Y. Yang, C.-W. Hsu, P.-Y. Chiu, Experimental study on the hydrogen charge and discharge rates of metal hydride tanks using heat pipes to enhance heat transfer, Appl. Energy 103 (2013) 581–587.
[13] G. Mohan, M.P. Maiya, S.S. Murthy, Performance simulation of metal hydride hydrogen storage device with embedded filters and heat exchanger tubes, Int. J. Hydrog. Energy 32 (2007) 4978–4987.
[14] Z. Wu, F. Yang, Z. Zhang, Z. Bao, Magnesium based metal hydride reactor incorporating helical coil heat exchanger: simulation study and optimal design, Appl. Energy 130 (2014) 712–722.
[15] J.O. Jensen, A.P. Vestbø, Q. Li, et al., The energy efficiency of onboard hydrogen storage, J. Alloys Compd. 446–447 (2007) 723–728.
[16] S. Garrier, B. Delhomme, P. de Rango, P. Marty, D. Fruchart, S. Miraglia, A new MgH_2 tank concept using a phase-change material to store the heat of reaction, Int. J. Hydrog. Energy 38 (2013) 9766–9771.
[17] S. Mellouli, N. Ben Khedher, F. Askri, A. Jemni, S. Ben Nasrallah, Numerical analysis of metal hydride tank with phase change material, ApplThermEng 90 (2015) 674–682.
[18] A.A.R. Darzi, H.H. Afrouzi, A. Moshfegh, M. Farhadi, Absorption and desorption of hydrogen in long metal hydride tank equipped with phase change material jacket, Int. J. Hydrog. Energy 41 (2016) 9595–9610.
[19] H. El Mghari, J. Huot, J. Xiao, Analysis of hydrogen storage performance of metal hydride reactor with phase change materials, Int. J. Hydrog. Energy 44 (2019) 28893–28908.
[20] L. Tong, J. Xiao, P. Bénard, R. Chahine, Thermal management of metal hydride hydrogen storage reservoir using phase change materials, Int. J. Hydrog. Energy 44 (2019) 21055–21066.
[21] H. Ben Maad, F. Askri, S. Ben Nasrallah, Heat and mass transfer in a metal hydrogen reactor equipped with a phase-change heat-exchanger, Int J Thermal Sciences 99 (2016) 271–278.
[22] H. Ben Mâad, F. Askri, J. Virgone, S. Ben Nasrallah, Numerical study of high-temperature metal-hydrogen reactor (Mg_2Ni-H_2) with heat reaction recovery using phase-change material during desorption, Appl. Therm. Eng. 140 (2018) 225–234.
[23] N.S. Nyamsi, I. Tolj, M. Lototskyy, Metal hydride beds-phase change materials: dual mode thermal energy storage for medium-high temperature industrial waste heat recovery, Energies 12 (2019) 3949–3972.
[24] A. Miled, S. Mellouli, Ben Maad, F. Askri, Improvement of the performance of metal hydride pump by using phase change heat exchanger, Int. J. Hydrog. Energy 42 (2017) 26343–26361.
[25] J. Yao, P. Zhu, L. Guo, L. Duan, Z. Zhang, S. Kurko, Z. Wu, A continuous hydrogen absorption/desorption model for metal hydride reactor coupled with PCM as heat management and its application in the fuel cell power system, Int. J. Hydrog. Energy 45 (2020) 28087–28099.
[26] Y. Ye, J. Lu, J. Ding, W. Wang, J. Yan, Numerical simulation on the storage performance of a phase change materials based metal hydride hydrogen storage tank, Appl. Energy 278 (2020), 115682.
[27] T. Alqahtani, A. Bamasag, S. Mellouli, F. Askri, P.E. Phelan, Cyclic behaviors of a novel design of a metal hydride reactor encircled by cascaded phase change materials, Int. J. Hydrog. Energy 45 (2020) 32285–32297.
[28] J. Lizana, R. Chacartegui, A. Barrios-Padura, J.M. Valverde, Advances in thermal energy storage materials and their applications towards zero energy buildings: a critical review, ApplEnerg 203 (2017) 219–239.
[29] Z. Ling, J. Chen, T. Xu, X. Fang, X. Gao, Z. Zhang, Thermal conductivity of an organic phase change material/expanded graphite composite across phase change temperature range and a novel thermal conductivity model, Energy Convers. Manag. 102 (2015) 202–208.
[30] R.J. Warzoha, R.M. Weigand, A.S. Fleischer, Temperature-dependent thermal properties of a paraffin phase change material embedded with herringbone style graphite nanofibers, Appl. Energy 137 (2015) 716–725.
[31] A. Chibani, S. Merouani, C. Cherif Bougriou, A. Dehane, Heat and mass transfer characteristics of charging in a metal hydride-phase change material reactor with nano oxide additives: the large scale-approach, Appl. Therm. Eng. 213 (2022), 118622.
[32] S. Wu, T. Yan, Z. Kuai, W. Pan, Thermal conductivity enhancement on phase change materials for thermal energy storage: a review, Energy Storage Materials 25 (2020) 251–295.

[33] H. Zheng, C. Wang, Q. Liu, Z. Tian, X. Fan, Thermal performance of copper foam/paraffin composite phase change material, Energy Convers. Manag. 157 (2018) 372–381.
[34] E. Fleming, S. Wen, L. Shi, A.K. Silva, Experimental and theoretical analysis of an aluminum foam enhanced phase change thermal storage unit, Int. J. Heat Mass Transf. 82 (2015) 273–281.
[35] X. Yang, P. Wei, X. Cui, L. Jin, Y.L. He, Thermal response of annuli filled with metal foam for thermal energy storage: an experimental study, Appl. Energy 250 (2019) 1457–1467.
[36] X. Yang, Z. Lu, Q. Bai, Q. Zhang, L. Jin, J. Yan, Thermal performance of a shell-and-tube latent heat thermal energy storage unit: role of annular fins, Appl. Energy 202 (2017) 558–570.
[37] A. Erek, Z. Ilken, M.A. Acar, Experimental and numerical investigation of thermal energy storage with a finned tube, Int. J. Energy Res. 29 (2005) 283–301.
[38] X. Zhai, X. Cheng, C. Wang, R. Wang, Experimental investigation and performance analysis of a fin tube phase change cold storage unit for high temperature cooling application, Energy Build 89 (2015) 9–17.
[39] M.K. Rathod, J. Banerjee, Thermal performance enhancement of shell and tube Latent Heat Storage Unit using longitudinal fins, ApplThermEng 75 (2015) 1084–1092.
[40] Y. Huang, Q. Sun, F. Yao, C. Zhang, C., Performance optimization of a finned shell-and-tube ice storage unit, Appl. ThermEng 167 (2020), 114788.
[41] C. Zhao, M. Opolot, M. Liu, F. Bruno, S. Mancin, K. Hooman, Numerical study of melting performance enhancement for PCM in an annular enclosure with internal-external fins and metal foams, Int. J. Heat Mass Transf. 150 (2020), 119348.
[42] Nabeel S. Dhaidan, J.M. Khodadadi, Improved performance of latent heat energy storage systems utilizing high thermal conductivity fins: a review, Journal of Renewable and Sustainable Energy 9 (2017), 034103, https://doi.org/10.1063/1.4989738.
[43] W.Q. Li, Z.G. Qu, Y.L. He, W.Q. Tao, Experimental and numerical studies on melting phase change heat transfer in open-cell metallic foams filled with paraffin, Appl. Therm. Eng. 37 (2012) 1–9.
[44] N. Sharifi, T.L. Bergman, A. Faghri, Enhancement of PCM melting in enclosures with horizontally-finned internal surfaces, Int. J. Heat Mass Transf. 54 (2011) 4182–4192.
[45] N.H.S. Tay, M. Belusko, A. Castell, L.F. Cabeza, F. Bruno, An effectiveness-NTU technique for characterising a finned tubes PCM system using a CFD model, Appl. Energy 131 (2014) 377–385.
[46] S. Nyallang Nyamsi, I. Tolj, M.J. Geca, Dehydrogenation of metal hydride reactor-phase change materials coupled with light-duty fuel cell vehicles, Energies 15 (2022) 2982.
[47] S.D. Lewis, P. Chippar, Analysis of heat and mass transfer during charging and discharging in a metal hydride - phase change material reactor, J. Energy Storage 33 (2021), 102108.
[48] N.S. Nyallang, M. Lototskyy, I. Tolj, Optimal design of combined two-tank latent and metal hydrides-based thermochemical heat storage systems for high-temperature waste heat recovery, Energies 13 (2020) 4216.
[49] R. Elarem, T. Alqahtani, S. Mellouli, A. Edacherian, F. Askri, A. Jemni, Numerical analysis of a built-in thermal storage system of metal hydride and nanoparticles enhanced phase change material and nanofluid, Int. J. Energy Res. 45 (2021) 5881–5893.
[50] H. El Mghari, J. Huot, L. Tong, J.S. Xiao, Selection of phase change materials, metal foams and geometries for improving metal hydride performance, Int. J. Hydrog. Energy 45 (2020) 14922–14939.
[51] M.W. Davids, M. Lototskyy, B.G. Pollet, Manufacturing of hydride-forming alloys from mixed titanium-iron oxide, Adv. Mater. Res. 746 (2013) 14–22.
[52] L. Pickering, M.V. Lototskyy, M.W. Davids, C. Sita, V. Linkov, Induction melted AB2-type metal hydrides for hydrogen storage and compression applications, Materials Today: Proceedings 5 (2018) 10470–10478.
[53] Saleel C. Ahamed, A review on the use of coconut oil as an organic phase change material with its melting process, heat transfer, and energy storage characteristics, J Thermal Analysis & Calorimetry 147 (2022) 4451–4472.
[54] Satya Sekhar Bhogilla, Design of an AB2-metal hydride cylindrical tank for renewable energy storage, J Energy Storage 14 (2017) 203–210.
[55] M. Visaria, I. Mudawar, T. Pourpoint, Enhanced heat exchanger design for hydrogen storage using high-pressure metal hydride: part 1. Design methodology and computational results. Int, J. Heat Mass Transf. 54 (2011) 413–423.
[56] R. Arora, S.C. Kaushik, R. Kumar, R. Arora, Soft computing based multi-objective optimization of Brayton cycle power plant with isothermal heat addition using evolutionary algorithm and decision making, Appl.Soft Comput. 46 (2016) 267–283.
[57] S.A. Mostafavi, Z. Hajabdollali, A. Ilinca, Multi-objective optimization of metal hydride hydrogen storage tank with phase change material, Therm Sci. Eng. Prog. 36 (2022), 101514.